# Numerical Modeling of Air-Water Flows in Bubble Columns and Airlift Reactors

Allison F. Studley

Thesis submitted to the Faculty of the
Virginia Polytechnic Institute and State University
in partial fulfillment of the requirements for the degree of

Master of Science
in
Mechanical Engineering

Francine Battaglia, Chair
Clint Dancey
Christopher Roy

October 12, 2010
Blacksburg, Virginia

Keywords: two-phase flow, bubble column, airlift reactor, CFD

Numerical Modeling of Air-Water Flows in Bubble Columns and Airlift Reactors

Allison F. Studley

# Abstract

Bubble columns and airlift reactors were modeled numerically to better understand the hydrodynamics and analyze the mixing characteristics for each configuration. An Eulerian-Eulerian approach was used to model air as the dispersed phase within a continuous phase of water using the commercial software FLUENT. The Schiller-Naumann drag model was employed along with virtual mass and the standard $k - \epsilon$ turbulence model. The equations were discretized using the QUICK scheme and solved with the SIMPLE coupling algorithm. The flow regimes of a bubble column were investigated by varying the column diameter and the inlet gas velocity using two-dimensional simulations. The typical characteristics of a homogeneous, slug, and heterogeneous flow were shown by examining gas holdup. The flow field predicted using two-dimensional simulations of the airlift reactor showed a regular oscillation of the gas flow due to recirculation from the downcomer and connectors, whereas the bubble column oscillations were random and resulted in gas flow through the center of the column. The profiles of gas holdup, gas velocity, and liquid velocity showed that the airlift reactor flow was asymmetric and the bubble column flow was symmetric about the vertical axis of the column. The average gas holdup in a 10.2 cm diameter bubble column was calculated and the results for the two-dimensional simulation of varying inlet gas velocities were similar to published experimental results. The average gas holdup in the airlift reactor for the three-dimensional simulations compared well with the experiments, and the two-dimensional simulations underpredicted the average gas holdup.

# Contents

# List of Figures

# List of Tables

# Nomenclature

### Roman variables

| | |
|---|---|
| $d_b$ | characteristic bubble diameter |
| $h$ | height above inlet |
| $k$ | turbulent kinetic energy |
| $\vec{v}$ | velocity field |
| $x$ | location along diameter |
| $C_D$ | drag coefficient |
| $D$ | column diameter |
| $\vec{F}$ | external body force |
| $\vec{F}_{vm}$ | virtual mass force |
| $\vec{g}$ | gravity |
| $H$ | column height |
| $\bar{\bar{I}}$ | identity matrix |
| $K_{pq}$ | interphase momentum exchange coefficient |
| $P$ | pressure |
| $Re$ | Reynolds number |
| $U$ | superficial velocity |
| $V$ | velocity |
| $V$ | volume |

### Greek variables

| | |
|---|---|
| $\alpha$ | volume fraction |
| $\Delta$ | cell size |
| $\Delta t$ | time step |
| $\epsilon$ | turbulent dissipation rate |
| $\lambda$ | bulk viscosity |
| $\mu$ | shear viscosity |
| $\rho$ | density |

### Subscripts

| | |
|---|---|
| 0 | initial height |
| $c$ | bubble column |
| $d$ | downcomer |
| $g$ | gas phase |
| $l$ | liquid phase |
| $p$ | phase p |
| $q$ | phase q |
| $r$ | riser |

# Chapter 1. Introduction

## 1.1 Background and Theory

Bubble column reactors are often used in industry to develop and produce chemicals and fuels for use in chemical, biotechnology, and pharmaceutical processes. The reactors involve gas-liquid flows where the gas is dispersed as bubbles in a continuous volume of liquid. When reactants are introduced into the flow, the interaction of gas and liquid can cause chemical reactions. For complete reactions, a well-mixed process is essential, and the reactor may include baffles and stirrers to enhance mixing. However, these additional devices can be detrimental in shear-sensitive processes. For example, micro-organisms can be used to produce synthesis gas (syngas), but are sensitive to the shear stress exerted by a reactor with moving parts or operating at high velocities [3]. Airlift reactors offer an alternative design because they can be constructed without moving parts (e.g. stirrers). The design of an airlift reactor creates a feedback loop, discussed next, which in turn improves mixing of the gas and liquid.

A bubble column is a vertical column of liquid with gas introduced continuously at the bottom through a sparger. Bubbles form and travel upwards through the column due to the inlet gas velocity and buoyancy. Airlift reactors are similar to bubble columns but have additional features. Schematics of both of these types of reactors are shown in Figure 1.1. An external loop airlift reactor has another vertical column called the downcomer, which is connected to the main column called the riser by upper and lower horizontal connectors. With the addition of gas directly into the riser, the hydrostatic pressure is lower in the riser than in the downcomer and causes the liquid to circulate into the riser

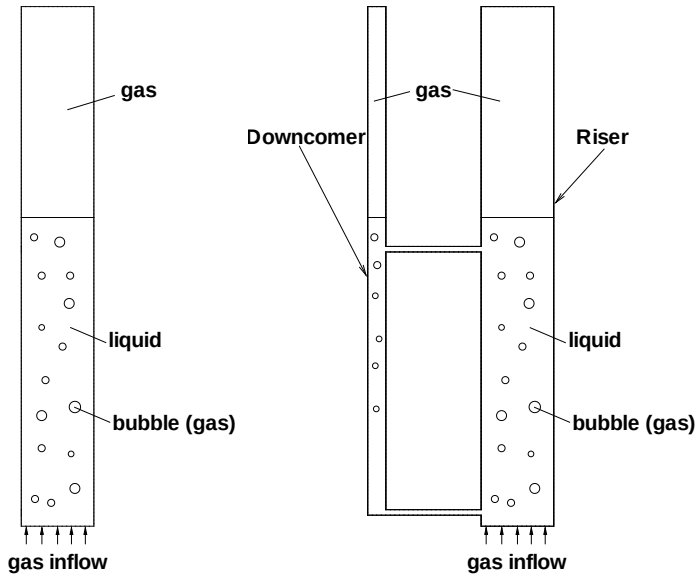


(a) (b)

Figure 1.1: Schematics for (a) bubble column and (b) external loop airlift reactor.

from the downcomer. The recirculation increases the liquid velocity of the riser without increasing the gas velocity at the sparger, which is helpful in biological applications where the material may be damaged under high stress. The type of operation used in airlift reactors is called semi-batch, where the fluids are not mixed initially and gas flows into the liquid. In contrast, a batch reactor is when gas and liquid are initially mixed and gas is released from the reaction.

Gas holdup $\alpha_g$ is the fraction of the total volume that is occupied by the gas. Because each phase occupies a portion of the total flow, a parameter called superficial velocity is introduced. Superficial velocity $U$ is related to the actual velocity $V$ (volumetric flow rate divided by the column cross-sectional area) by multiplying by the volume fraction of the individual phase $\alpha$. Gas holdup and superficial gas velocity are important parameters, which can affect the surface area of the bubbles and the amount of time the gas is present in the reactor, and in turn the mass transfer, which will affect the overall process [4]. In all gas-liquid flows, the bubbles can increase and decrease in size due to coalescence and breakup. Coalescence is two or more bubbles colliding, whereby the thin liquid barrier

between ruptures to form a larger bubble. Breakup of bubbles is caused by collisions with turbulent eddies, approximately equal in size to the bubbles [5].

The type of flow, or flow regime, also influences the hydrodynamics of the reactors and is highly dependent on the inlet gas velocity. Shah and Deckwer [2] studied the dynamics of gas-liquid flows in bubble columns and identified three flow regimes: bubbly or homogeneous flow, heterogeneous flow, and slug flow. Bubbly flow is found at low velocities and consists of small, similarly sized (homogeneous) bubbles. It was noted [2] that in the bubbly regime, there is little interaction between the bubbles and there is a maximum amount of gas that can be transported through the column. The maximum gas flowrate in the homogenous regime is called the flooding point, after which the amount of gas transported increases in the form of large bubbles and bubble clusters and the flow develops into heterogeneous or slug flow. Heterogeneous flow consists of differently sized bubbles and slug flow is when large bubbles form that span most of the column diameter.

## 1.2 Previous Studies

### 1.2.1 Computational Models

Bubble columns and airlift reactors have been studied in the past, both experimentally and computationally. Both of these techniques help advance the knowledge of the hydrodynamics and further use of these reactors. Computational fluid dynamics (CFD) models are developed and tested to determine their accuracy for predicting results obtained experimentally. Gas-liquid flows can be modeled using Eulerian-Lagrangian or Eulerian-Eulerian methods. In the Eulerian-Lagrangian method, only the liquid is treated as continuous, whereas the Eulerian-Eulerian method treats both phases as interpenetrating continua. The Eulerian-Lagrangian method is computationally intensive because each bubble is tracked in a Lagrangian framework. Thus, the more common model in CFD is the Eulerian-Eulerian method. Within the Eulerian-Eulerian method, there are

three approaches: (a) volume of fluid, (b) mixture, and (c) Eulerian. The volume of fluid model solves a single set of momentum equations for two or more fluids and tracks the volume fraction of each fluid throughout the domain. The mixture model solves for the momentum equation of the mixture and prescribes relative velocities to describe the dispersed phases. The Eulerian model solves momentum and continuity equations for each of the phases, and the equations are coupled through pressure and exchange coefficients. For the work herein, the commercial code FLUENT will be used to simulate gas-liquid flows. The Eulerian-Eulerian method will be used, and Chapter 2 provides more details related to the models.

Turbulence in bubbly flows is different from a single-phase flow in that it considers the relative motion of the two phases and the bubble induced drag, which is dependent on the bubble size [6]. There have been many researchers who have studied the use of turbulent models in gas-liquid flows [7–12]. It is well agreed on that the use of a turbulence model is appropriate but the standard $k-\epsilon$ model has limitations when used for gas-liquid flows. Schwarz et al. [12] tested the agreement of the standard constants $(C_1, C_2, C_3)$ of the $k-\epsilon$ turbulence model to a two-phase flow. They found that no change in the constants is needed to achieve agreement with experimental results. They determined that the standard $k-\epsilon$ model is appropriate for bubbly flows as long as separate momentum equations are solved for each phase and no assumptions are made about the void fraction distribution. Jakobsen et al. [6] used turbulence models to account for the recirculating flow and the large amount of interaction between bubbles. They reference that turbulence modeling is important to predict gas holdup, especially because the distribution of the phases is due to the turbulence of the continuous fluid phase (liquid).

Sato et al. [7] developed a bubble induced turbulence model which accounts for the wall turbulence present irrespective of the presence of bubbles and the turbulence caused by wakes of bubbles. This model is widely used [13, 14] as an alternative to the standard $k-\epsilon$ model.

Some researchers have looked at the near-wall effect of turbulence. Politano et al. [11] and Lopez de Bertodano [10] discovered that the logarithmic law of the wall used for single phase flow needs to be modified to be applied to two-phase flow. Politano et al. [11] used the standard $k-\epsilon$ model for single phase flow but developed a logarithmic law of the wall for two-phase flows. They did not specify no-slip conditions at the walls since the $k-\epsilon$ model is not valid in the near wall region. Lopez de Bertodano [10] used the single-phase logarithmic law of the wall but found it impractical to use the no-slip condition at the wall due to the small grid cell size needed. Sokolichin and Eigenberger [8] stated that the grid cell size for gas-liquid flows using the Euler-Euler method needs to be much larger than the size of a single bubble as well as small with respect to the total dimensions of the domain.

Law et al. [15] used FLUENT to simulate a bubble column flow for two- and three-dimensional models and tested the effects of different cell resolutions to predict average gas holdup. They were able to obtain close agreement between the two-dimensional simulations and experiments of Rampure et al. [16] with a cell size of 0.67 cm, and found that cell sizes smaller than the bubble diameter resulted in unrealistic solutions. The three-dimensional simulations with comparable resolution to the two-dimensional simulations predicted similar results. Law et al. also performed simulations for a two-dimensional bubble column using the code CFDLib [17]. The CFDLib solutions were compared with the FLUENT solutions [15] and finer grid resolutions were possible with CFDLib. Lopez de Bertodano [10] specified a velocity tangential to the wall at some distance away from the wall and the law of the wall is used in the "buffer zone" rather than stretching the cells near the wall. FLUENT is unable to specify any conditions other than at the boundaries (no-slip or specified shear stress at the walls) without the use of user-defined functions. Monahan et al. [13] used both free-slip and periodic boundary conditions at the walls in their simulations to diminish the effects of the wall.

Glover and Generalis [18] simulated two-dimensional bubble column flows using FLU-

ENT and employed the algebraic slip mixture model and modified scalar equation mixture model. They further investigated turbulence models and concluded that the Reynolds stress model corresponded better than the $k - \epsilon$ model to experimental data. Sari et al. [19] performed a similar study using FLUENT for both two- and three-dimensional domains and incorporated user-defined functions to model and test two different interphase momentum transfer mechanisms, the interfacial area transport equation and bubble number density approach. Their results showed that both transport models agreed with the experimental data and the three-dimensional simulations had better agreement than the two-dimensional simulations. Simcik et al. [20] used direct numerical simulations with the volume of fluid model in FLUENT to compute the constants for the added mass coefficient of particles in various configurations. They found that the constant can depend on the shape of the bubble (spherical or ellipsoidal) and the arrangement of the bubbles (e.g., single versus multiple and horizontal versus vertical movement).

Rampure et al. [16] performed experiments on a 20 cm cylindrical column, 2.0 m high and also simulated the setup in FLUENT. The experiments were carried out with both gas-liquid and gas-liquid-solid systems at velocities of 10 cm/s and 20 cm/s. They were limited to measuring only gas holdup and not velocity. Their computational results for gas holdup were higher than their measured values, but within acceptable agreement, with experimental error given as the possible reason for the difference.

### 1.2.2 Reactor Design

Ranade and Tayalia [21] simulated the effect of the sparger (gas inlet) design on a shallow bubble column. They saw more circulation with a double ring (0.45 m and 0.78 m diameter) sparger than a single ring (0.45 m diameter) and concluded that the use of a single or double ring had a significant effect on the amount of mixing in bubble columns with a maximum height to diameter ratio of 2:1. Gavrilescu and Tudose [22] performed experiments on an external loop airlift reactor. They looked at the area ratio of the

downcomer to riser and found that when the ratio was increased, the liquid circulation velocity increased, which in turn increased the riser gas holdup.

Vial et al. [23] performed experiments and simulations of an external loop airlift reactor with a 15 cm diameter riser, 8 cm diameter downcomer, and 6 m column height, with an initial water level high enough so that gas would not enter the downcomer. They looked at the effects of the amount the downcomer vent was opened, which is similar to reducing the diameter of the downcomer. They found that at low valve openings, the airlift reactor behaved nearly like a bubble column, gas holdup increased and liquid velocity decreased. However, the valve opening had little effect on openings greater than 70%.

## 1.3 Motivation and Objectives

Before building a full-scale reactor, which can be time consuming and expensive, it is useful to be able to simulate the gas-liquid interactions using CFD. The goal is to be able to correctly model bubble columns and airlift reactors using the commercial code FLUENT. In reality, the reactors are three-dimensional and can be occupied by various sizes of bubbles, both of which can be hard to correctly simulate in complex geometries. The complex geometry can increase the CPU time of a simulation. The 2D simulations can be helpful for scale-up and design of reactors if they provide similar results to the 3D simulations. The goal is to eventually simulate the chemical reactions that produce syngas. Before reactions can be simulated, the hydrodynamics must be shown to be correctly predicted and therefore an inert air-water system is studied.

The first objective is to examine the flow regimes and hydrodynamic characteristics of flow in a bubble column. Then two-dimensional models will be studied and compared with experimental data. Finally, three-dimensional models will be considered to determine if they significantly improve the results. Another issue is that the gas phase is

modeled discretely, so an effective bubble diameter is specified to represent the mean bubble size. There have been studies [14, 24, 25] which include a polydispersed model to account for the coalescence and breakup of bubbles, but such an approach will not be used here and will be left for future work. To account for the change in bubble sizes as the flow crosses into different flow regimes without employing a polydispersed model, the effective bubble size will be increased at higher velocities.

The remainder of the thesis will be presented as follows. The governing equations and discretization are described in Chapter 2. These equations include conservation of mass and momentum as well as other interfacial terms necessary for two-phase flows. Results are presented in Chapters 3 and 4 for simulations of a bubble column and airlift reactor, respectively. Qualitative mixing results are presented and then models are validated with experiments. Finally, suggestions for future work beyond the current investigation are discussed.

# Chapter 2. Numerical Formulations

An Eulerian multiphase flow model will be used to describe the gas and liquid phases of bubble column flows. The system is considered to be a continuum with averaged transport equations for each phase. The Eulerian model employed by ANSYS FLUENT 12.0 is used to perform the simulations. This chapter will elaborate on the governing equations and discretization techniques.

## 2.1 Governing Equations

The Eulerian multiphase model allows for multiple interacting phases by assuming that each phase behaves as interpenetrating continua. Phasic volume fractions describe the region occupied by each phase and are incorporated into the conservation equations for mass and momentum. The phasic volume fraction $\alpha$ must satisfy the relation:

$$\sum_{q=1}^{n} \alpha_q = 1 \tag{2.1}$$

where $n$ is the total number of phases. The conservation equations are written by performing an ensemble average of the local instantaneous balance for each phase. Only two phases are needed to describe gas-liquid flows, $n = 2$. The liquid is modeled as the continuous (primary) phase and the gas is modeled as the dispersed (secondary) phase.

The continuity equation for phase $q$ is:

$$\frac{\partial}{\partial t}(\alpha_q \rho_q) + \nabla \cdot (\alpha_q \rho_q \vec{v}_q) = 0 \tag{2.2}$$

where $\rho$ is the density and $\vec{v}$ is the velocity field. The right hand side is zero because applications in this research do not involve mass transfer or reactions.

The momentum equation for phase $q$ is:

$$\frac{\partial}{\partial t}(\alpha_q \rho_q \vec{v}_q) + \nabla \cdot (\alpha_q \rho_q \vec{v}_q \vec{v}_q) = -\alpha_q \nabla P + \nabla \cdot \bar{\bar{\tau}}_q + \alpha_q \rho_q \vec{g} + \sum_{p=1}^{n} K_{pq}(\vec{v}_p - \vec{v}_q) + (\vec{F}_q + \vec{F}_{vm,q}) \quad (2.3)$$

and the subscript $p$ denotes the second phase. The terms on the right hand side include the pressure shared by all phases, $P$, the stress-strain tensor, $\bar{\bar{\tau}}_q$, the interphase momentum exchange coefficient, $K_{pq}$, the external body force, $\vec{F}_q$, and the virtual mass force, $\vec{F}_{vm,q}$. The stress-strain tensor is defined as:

$$\bar{\bar{\tau}}_q = \alpha_q \mu_q (\nabla \vec{v}_q + \nabla \vec{v}_q^T) + \alpha_q (\lambda_q - \frac{2}{3}\mu_q) \nabla \cdot \vec{v}_q \bar{\bar{I}} \quad (2.4)$$

where $\mu_q$ and $\lambda_q$ are the shear and bulk viscosity of phase $q$, $\nabla \vec{v}_q^T$ is the transpose of the velocity gradient, and $\bar{\bar{I}}$ is the identity matrix.

The interphase exchange coefficient, $K_{pq}$, for gas-liquid flows is determined by the drag function. The Schiller-Naumann drag model will be used and is generally acceptable for all multiphase calculations [1]. The general form of the interphase exchange coefficient is:

$$K_{pq} = \frac{\alpha_q \alpha_p \rho_p C_D Re}{24 \tau_p} \quad (2.5)$$

where $Re$ is the relative Reynolds number, defined as:

$$Re = \frac{\rho_q |\vec{v}_p - \vec{v}_q| d_p}{\mu_q} \quad (2.6)$$

where $\vec{v}_p - \vec{v}_q$ is the slip velocity of the two phases and $d_p$ is the effective (characteristic) bubble diameter. The particulate relaxation time $\tau_p$ is:

$$\tau_p = \frac{\rho_p d_p^2}{18 \mu_q} \quad (2.7)$$

The drag coefficient $C_D$ is defined by Schiller and Naumann as [26]:

$$C_D = \begin{cases} 24(1 + 0.15Re^{0.687})/Re & Re \leq 1000 \\ 0.44 & Re > 1000 \end{cases} \tag{2.8}$$

Virtual mass, also called added mass, is the mass that must be accounted for due to the no-slip interaction of the two phases and virtual mass is included in the momentum equation (2.3). Physically, the virtual mass represents how the gas bubble will accelerate or move some of the surrounding liquid when the bubble moves [27]. The virtual mass is important due to the large difference in densities of the two phases [1]. The virtual mass force is defined as:

$$\vec{F}_{vm,p} = 0.5\alpha_p\rho_q \left( \frac{D_q\vec{v}_q}{Dt} - \frac{D_p\vec{v}_p}{Dt} \right) \tag{2.9}$$

and $\frac{D}{Dt}$ is the substantial derivative. This model is used by Monahan et al. [13], Law et al. [15], Simcik et al. [20], Sanyal et al. [25], among many others.

The standard $k-\epsilon$ dispersed turbulence model is a modified version of the turbulent kinetic energy, $k$, and dissipation rate, $\epsilon$, to account for the two phases:

$$\frac{\partial}{\partial t}(\alpha_q\rho_q k_q) + \nabla\cdot(\alpha_q\rho_q\vec{v}_q k_q) = \nabla\cdot(\alpha_q\frac{\mu_{t,q}}{\sigma_k}\nabla k_q) + \alpha_q G_{k,q} - \alpha_q\rho_q\epsilon_q + \alpha_q\rho_q\Pi_{kq} \tag{2.10}$$

$$\frac{\partial}{\partial t}(\alpha_q\rho_q\epsilon_q) + \nabla\cdot(\alpha_q\rho_q\vec{v}_q\epsilon_q) = \nabla\cdot(\alpha_q\frac{\mu_{t,q}}{\sigma_\epsilon}\nabla\epsilon_q) + \alpha_q\frac{\epsilon_q}{k_q}(C_{1\epsilon}G_{k,q} - C_{2\epsilon}\rho_q\epsilon_q) + \alpha_q\rho_q\Pi_{\epsilon_q} \tag{2.11}$$

where $G_{k,q}$ is the production of turbulent kinetic energy, $\mu_t$ is turbulent viscosity, and $C_{1\epsilon}, C_{2\epsilon}$ are constants equal to 1.44 and 1.92, respectively. The terms $\Pi_{kq}$ and $\Pi_{\epsilon_q}$ represent the influence of the dispersed phase $p$ on the continuous phase $q$, defined as:

$$\Pi_{kq} = \sum_{p=1}^{M} \frac{K_{pq}}{\alpha_q\rho_q}(k_{pq} - 2k_q + |\vec{v}_p - \vec{v}_q|\cdot\vec{v}_{dr}) \tag{2.12}$$

$$\Pi_{\epsilon q} = C_{3\epsilon}\frac{\epsilon_q}{k_q}\Pi_{kq} \tag{2.13}$$

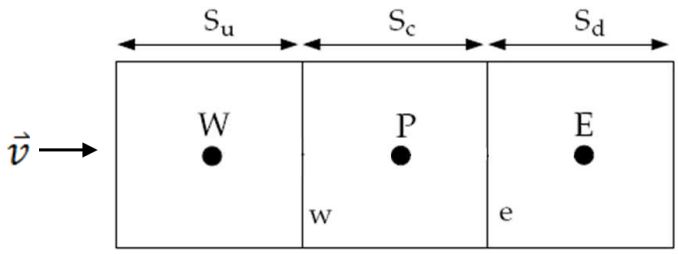


Figure 2.1: Example of one-dimensional control volume used in QUICK discretization [1] with the flow direction denoted by $\vec{v}$.

where $k_{pq}$ is the covariance of the velocities of the phases $q$ and $p$, $\vec{v}_{dr}$ is the drift velocity, and $C_{3\epsilon}$ is a constant equal to 1.2.

## 2.2 Discretization

For spatial discretization, the quadratic upwind interpolation for convective kinematics (QUICK) scheme [28] is used, which is based on a weighted average of second-order upwind and central interpolations of the dependent variables. The generic variable $\phi$ is solved at face $e$ by:

$$\phi_e = \theta \left[ \frac{S_d}{S_c + S_d}\phi_P + \frac{S_c}{S_c + S_d}\phi_E \right] + (1-\theta) \left[ \frac{S_u + 2S_c}{S_u + S_c}\phi_P + \frac{S_c}{S_u + S_c}\phi_W \right] \tag{2.14}$$

where the subscripts u, c, and d refer to the upwind, center, and downwind cells, as shown in Figure 2.1. Each cell has a size $S$ and variable $\phi$ is stored at the cell center. For example, $P$ is the cell center for the middle cell, $W$ is the cell center for the upwind cell, and $E$ is the cell center for the downwind cell. The variable $\theta$ represents the interpolation scheme, where $\theta = 1$ results in a central second-order interpolation and $\theta = 0$ is second-order upwind. The QUICK scheme works best with structured meshes and for non-hexahedral or non-quadrilateral cells in unstructured meshes, $\theta = 0$.

The first order implicit time discretization is written as:

$$\frac{\phi^{n+1} - \phi^n}{\Delta t} = F(\phi^{n+1}) \tag{2.15}$$

where $F$ is any spatial discretization of scalar quantity $\phi$ and $n$ is the current time step.

## 2.3 Solver Algorithm

The pressure-based solver uses the phase coupled semi-implicit method for pressure linked equations (SIMPLE) pressure-velocity coupling algorithm [29]. In the SIMPLE algorithm, an initial pressure field is guessed to calculate the velocity using the momentum equation and then both the pressure and velocity terms are corrected in order to satisfy the continuity equation. The actual pressure $P$ and velocity $v$ are calculated by:

$$P = P_0 + \beta_P P' \tag{2.16}$$

$$v = v_0 + v' \tag{2.17}$$

where $P_0$ and $v_0$ are the guessed (or intermediate) values of pressure and velocity, $\beta_P$ is the under-relaxation factor for pressure which helps the rate of convergence, and $P'$ and $v'$ are the corrections for pressure and velocity. The pressure and velocity corrections are related by an approximate form of the momentum equation, written as:

$$v' = -A\frac{\partial P'}{\partial x} \tag{2.18}$$

where $A$ is a fictitious time increment divided by density which includes the momentum under-relaxation factor. The velocity estimation and velocity correction equations (2.17,

2.18) are then combined to find the pressure correction term:

$$-\frac{\partial v_0}{\partial x} + A\frac{\partial^2 P'}{\partial x^2} = 0 \tag{2.19}$$

The pressures and velocities are continually guess-and-corrected until the solution converges.

## 2.4 Variable Definitions and Boundary Conditions

The gas velocity at the inlet (sparger) is defined as the volumetric flow rate divided by the total cross-sectional area of the sparger. The superficial velocity $U$ is the phase velocity $V$ multiplied by the volume fraction $\alpha$:

$$U = \alpha V \tag{2.20}$$

where the volume fraction is the ratio of the phase volume to the total volume. For example, the gas volume fraction (or gas holdup) is defined as:

$$\alpha_g = \frac{V_g}{V_g + V_l} \tag{2.21}$$

The superficial gas velocity at the inlet is equal to the gas velocity at the inlet because volume fraction of the gas through the sparger is 1.

The boundaries of the bubble column are either an inlet, outlet, or wall. The inlet is specified with gas at a uniform velocity and a volume fraction of 1 and the outlets have a pressure equal to atmospheric. The turbulent kinetic energy and dissipation rate are set to 0 at the inlets and outlets because the effects of turbulence at the boundaries are difficult to approximate. The walls are specified with a no-slip condition for the gas and liquid phases. Futher details will be provided in the results and discussion.

# Chapter 3. Bubble Column

## 3.1 Effects of Modeling Parameters

### 3.1.1 Grid Resolution and Bubble Diameter

A grid resolution study was performed to find the best cell size for the gas-liquid simulations. The grids were created in ANSYS ICEM CFD 12 and imported into ANSYS FLUENT 12. The test cases were performed in a column with diameter $D_c = 20$ cm and column height $H_c = 200$ cm with a static liquid height $h_0 = 100$ cm and an inlet gas velocity $U_g = 10$ cm/s, as defined in Figure 3.1. Six grid sizes were tested using an effective bubble diameter of $d_b = 0.5$ cm: $10 \times 100$, $20 \times 200$, $30 \times 300$, and $40 \times 40$, which correspond to cell sizes $\Delta = 2$ cm, 1 cm, 0.67 cm, 0.5 cm, 0.33 cm, and 0.25 cm. The size of the cell in both the $x$- and $y$-directions was specified with a 1:1 ratio. The time step was decreased with decreasing cell size to help maintain numerical stability. In addition, six grid resolutions were tested using an effective bubble diameter of $d_b = 1.0$ cm: $\Delta = 2.5$ cm, 2 cm, 1.54 cm, 1 cm, 0.77 cm, 0.5 cm, to see the effect of increasing the bubble diameter with respect to grid resolution. A summary of the cases are shown in Table 3.1 and includes whether the solutions converged (C) or diverged (D). The simulations for grid cells that are significantly smaller than the bubble diameter become unstable irrespective of the time step. The dependency of cell size relative to bubble size shown here is similar to the findings by Law et al. [15] and Sokolichin and Eigenberger [8].

The results for gas holdup and liquid velocity are averaged from $5 - 65$ s with 6,000 time realizations. Profiles for average gas holdup and liquid velocity at heights of $h = 15$

Table 3.1: Grid cell sizes ($\Delta$) and effective bubble diameters for different time steps ($\Delta t$). C indicates a converged solution, D indicates a diverged solution, and "-" indicates those parameters were not tested.

| $d_b$ (cm) | $\Delta$ (cm) | $\Delta t$ (s) | | | |
|---|---|---|---|---|---|
| | | 0.01 | 0.005 | 0.001 | 0.0005 |
| 0.5 | 2 | C | C | - | - |
| | 1 | - | C | - | - |
| | 0.67 | - | C | C | C |
| | 0.5 | - | C | C | - |
| | 0.33 | - | D | D | D |
| | 0.25 | - | - | D | D |
| 1.0 | 2.5 | - | C | - | - |
| | 2 | - | C | - | - |
| | 1.54 | - | C | - | - |
| | 1 | - | C | - | - |
| | 0.77 | - | D | C | C |
| | 0.5 | - | D | D | D |

and 65 cm from the inlet for the converged solutions of $d_b = 0.5$ cm are shown in Figures 3.2 and 3.3. The gas holdup is compared to experimental data of Rampure et al. [16]. For the effective bubble diameter of 0.5 cm, cells significantly larger ($\Delta = 2$ cm, 1 cm) than the bubble diameter result in unphysical gas holdup solutions (Figure 3.2) and $\Delta = 1$ cm results in an expected parabolic liquid velocity profile (Figure 3.3). The cell size equal to the bubble diameter ($\Delta = 0.5$ cm) does not provide physical solutions for either gas holdup or liquid velocity. The $\Delta = 0.67$ cm grid cell size results in the best gas holdup comparison to the experimental results and a parabolic velocity profile. In order to account for a larger bubble diameter, a larger cell size would be needed. Profiles for average gas holdup and liquid velocity at heights of $h = 15$ and 65 cm from the inlet for the converged solutions of $d_b = 1$ cm are shown in Figures 3.4 and 3.5. Similar to the results for $d_b = 0.5$ cm, cell sizes close to or smaller ($\Delta = 1$ cm, 0.77 cm) than the bubble diameter as well as significantly larger ($\Delta = 2.5$ cm) than the bubble diameter provide unphysical solutions. The cell sizes of 1.54 and 2 cm result in slightly better solutions, however the choice in bubble diameter represents an unphysical situation and therefore it is not surprising that a good solution is not obtained.

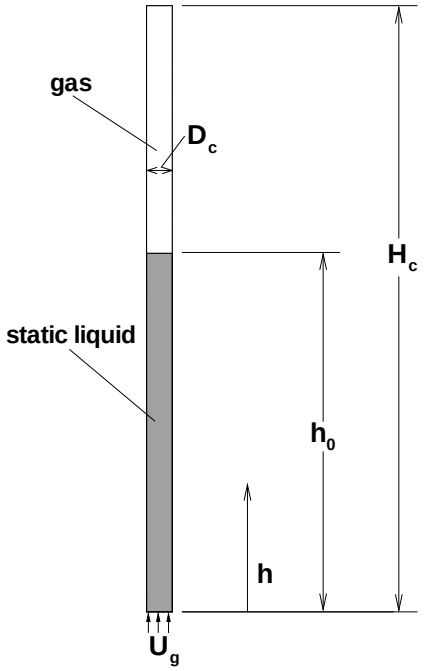


Figure 3.1: Schematic and variable definitions for a bubble column.

A Richardson extrapolation [30] was performed to estimate the amount of relative discretization error on the grid of $\Delta = 0.67$ cm and $d_b = 0.5$ cm. The exact solution for dependent variable $\psi$ can be estimated from solutions obtained with a fine and coarse grid whose cell size differ by a factor of 1.5 using [31]:

$$\psi_{exact} = \psi_{fine} + \frac{\psi_{fine} - \psi_{coarse}}{1.25} \tag{3.1}$$

and the relative discretization error (RDE) is determined by:

$$RDE_{fine} = \frac{\psi_{fine} - \psi_{exact}}{\psi_{exact}} \tag{3.2}$$

The relative discretization error found for the $30 \times 300$ grid ($\Delta = 0.67$ cm) was 7.3% for $\alpha_g$ and 4.2% for $V_l$.

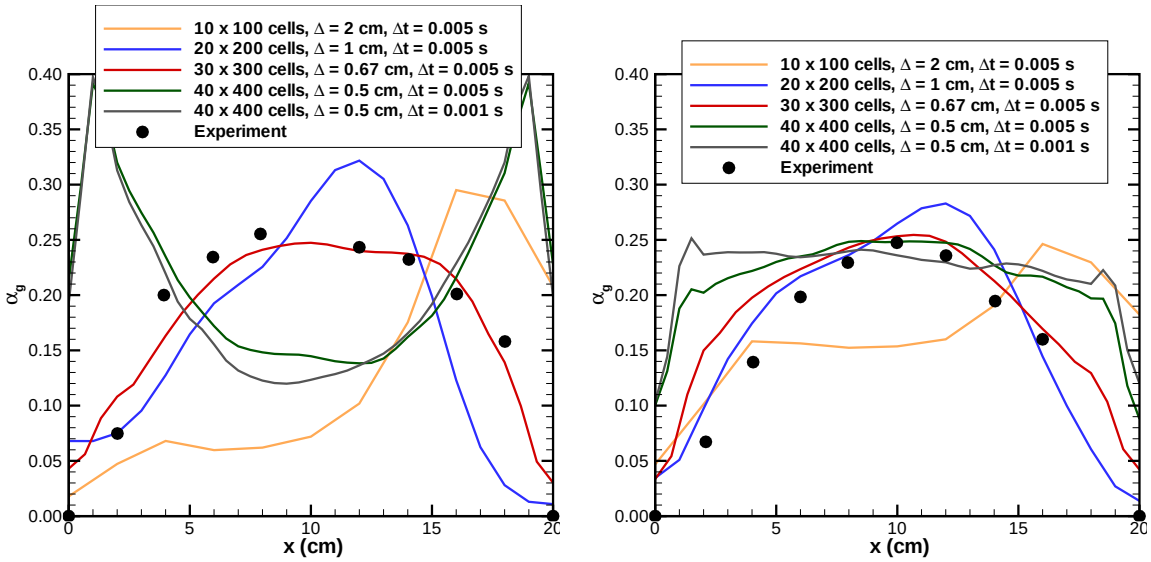


(a) (b)

Figure 3.2: Grid resolution study comparing profiles for gas holdup at (a) h = 15 cm and (b) h = 65 cm. Effective bubble diameter, $d_b = 0.5$ cm.

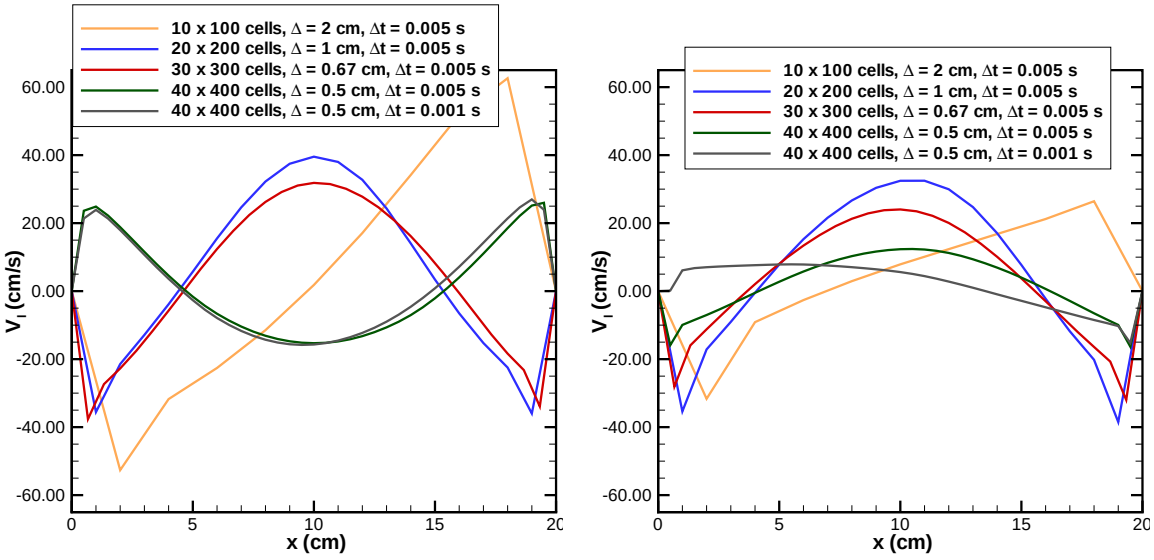


(a) (b)

Figure 3.3: Grid resolution study comparing profiles for liquid velocity at (a) h = 15 cm and (b) h = 65 cm. Effective bubble diameter, $d_b = 0.5$ cm.

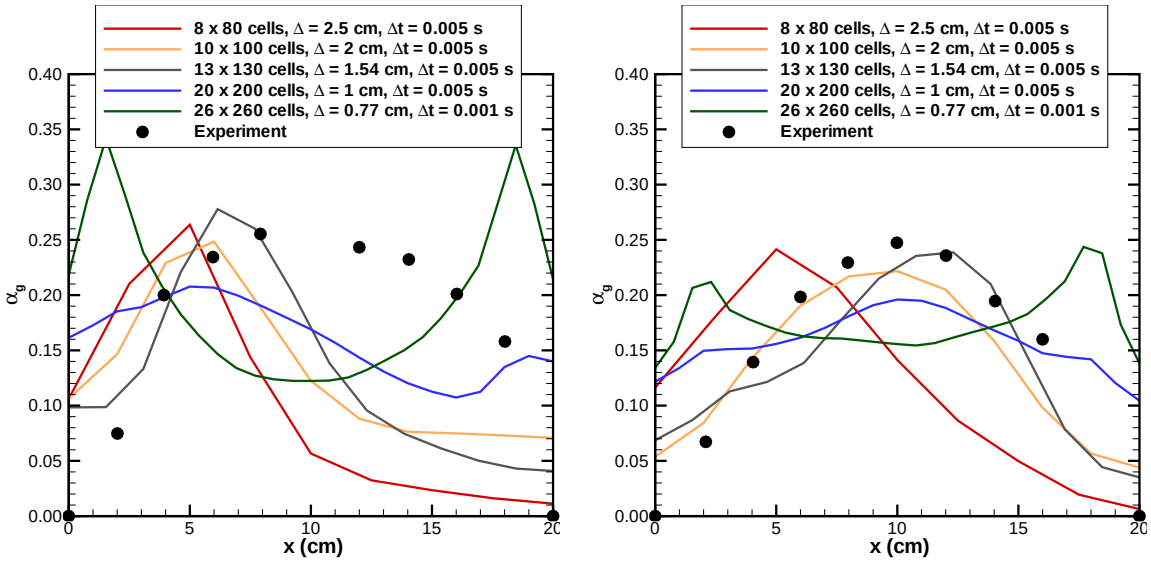


(a) (b)

Figure 3.4: Grid resolution study comparing profiles for gas holdup at (a) h = 15 cm and (b) h = 65 cm. Effective bubble diameter, $d_b = 1$ cm.

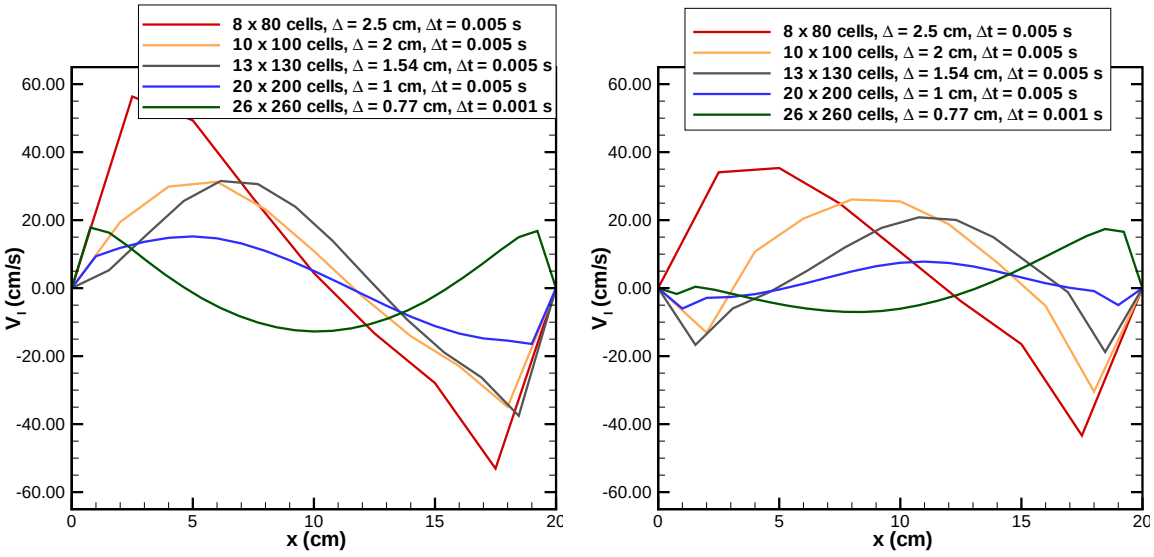


(a) (b)

Figure 3.5: Grid resolution study comparing profiles for liquid velocity at (a) h = 15 cm and (b) h = 65 cm. Effective bubble diameter, $d_b = 1$ cm.

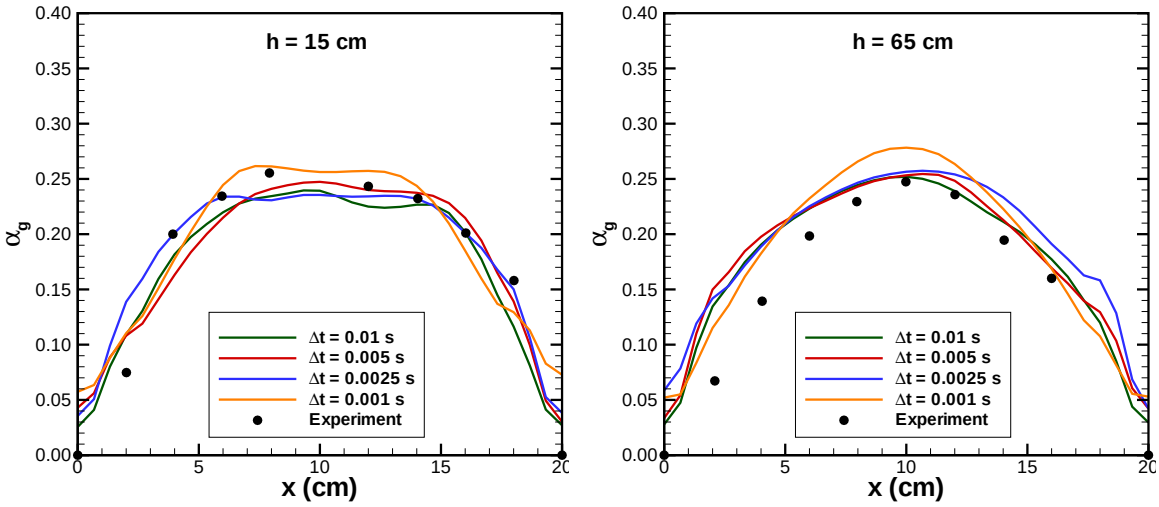


(a) (b)

Figure 3.6: Time step study comparing profiles for gas holdup at (a) h = 15 cm and (b) h = 65 cm, with $d_b = 0.5$ cm, $\Delta = 0.67$ cm.

### 3.1.2 Time Step

Four time steps, $\Delta t$ = 0.01 s, 0.005 s, 0.0025 s, and 0.001 s, were tested using $\Delta = 0.67$ cm with effective bubble diameter $d_b = 0.5$ cm to assess the effects of time step $\Delta t$ on the solution. The definition of $CFL = \frac{U_g \Delta t}{\Delta} = 1$ is often used in single phase flows to find an appropriate $\Delta t$ for a simulation based on the discretization method. However this definition is inappropriate for two-phase flows and the resulting $\Delta t = 0.067$ s would result in numerical instabilities. The average gas holdup profiles for inlet gas velocity $U_g$ = 10 cm/s at $h$ = 15 cm and 65 cm are shown in Figure 3.6. All time steps have a flat region near the middle of the column at $h$ = 15 cm due to the flow not being fully developed. The smallest time step, $\Delta t$ = 0.001 s, overpredicts the gas holdup at $h$ = 65 cm, whereas the other time steps give comparable results. Time steps of $\Delta t$ = 0.01 s, 0.005 s, 0.001 s, 0.0005 s, and 0.0001 s were also tested using a $2^{nd}$ order time discretization scheme and all cases resulted in a diverged solution.

The convergence criteria for the 2D case was set to $10^{-4}$ and 200 maximum pseudo-

Table 3.2: CPU requirements for 2D and 3D BC simulations.

| | 2D | 3D |
|---|---|---|
| CPU (h) | 17.5 | 402.6 |
| # time steps | 14,000 | 140,000 |
| $\Delta t$ (s) | 0.005 | 0.0005 |
| # cells | 5,295 | 64,952 |
| CPU/timestep/cell ($\mu s$) | 850 | 159 |

iterations per time step. The convergence criteria for the 3D case, presented later in this chapter, was increased to $10^{-3}$ due to the large CPU time required to reach the convergence of $10^{-4}$. The 3D case used a time step of $\Delta t = 0.0005$ s for better stability and was set to 100 maximum pseudo-iterations per time step. The CPU requirements for a typical 2D and 3D case are shown in Table 3.2. The 2D case required 23 times less total CPU time than the 3D case but the CPU/timestep/cell was 5 times greater.

### 3.1.3 Turbulence

In order to test the appropriateness of using a turbulence model on the gas-liquid flow, a sample case was run without the standard $k - \epsilon$ model, effectively creating a laminar model. The bubble column simulation specified an inlet gas velocity of $U_g = 10$ cm/s and a time step of $\Delta t = 0.0025$ s. Time-averaged gas holdup for both models are shown in Figure 3.7 and shows that the laminar model results in an unphysical solution. The gas holdup predictions show two concentrated regions of high gas flow in the lower half of the column (below $h = 50$ cm). In contrast, the flow field predicted using the (recommended) turbulence model develops into a more homogeneous flow, as to be expected.

## 3.2 Flow Regimes

In an effort to better understand the bubble dynamics, flows can be characterized into different types, or regimes. These regimes depend on the column diameter and inlet gas velocity. Knowing the flow regime is helpful in predicting certain results and can

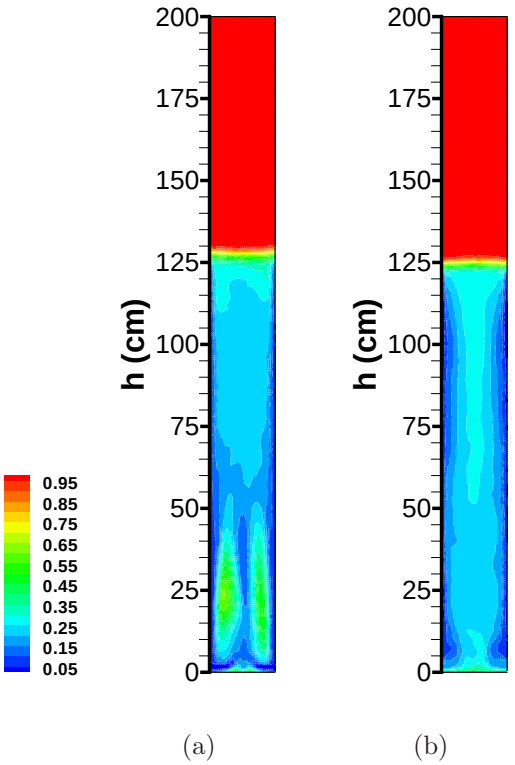


Figure 3.7: Average gas holdup contours for $U_g = 10$ cm/s, $\Delta t = 0.0025$ s using the (a) laminar model and the (b) $k - \epsilon$ turbulence model.

help with specifying numerical models such as mean bubble diameter. Three regimes are possible, bubbly or homogeneous flow, slug flow, and heterogeneous flow. Shah and Deckwer [32] categorized gas flow rates that are most common as a flow regime map, which is reproduced in Figure 3.8. As shown in Figure 3.8, inlet gas flows up to 3 - 4 cm/s are characterized by a bubbly homogeneous flow, irrespective of column diameter. Above 7 cm/s, increasing the column diameter will cause the flow to go from slug, transitional, and then heterogeneous flow. Bubbly flow is defined by uniform bubbles at a size determined by the flow through the sparger. Slug flow produces large bubbles that can take up the entire diameter of the column. In small diameter columns at higher velocities, large bubbles become stabilized by the column walls which form slugs. Bubbles and bubble clusters can form up to 10 cm in diameter and slugs will generally not form in columns larger than 15 cm [2]. Heterogeneous flow comprises bubbles of different sizes

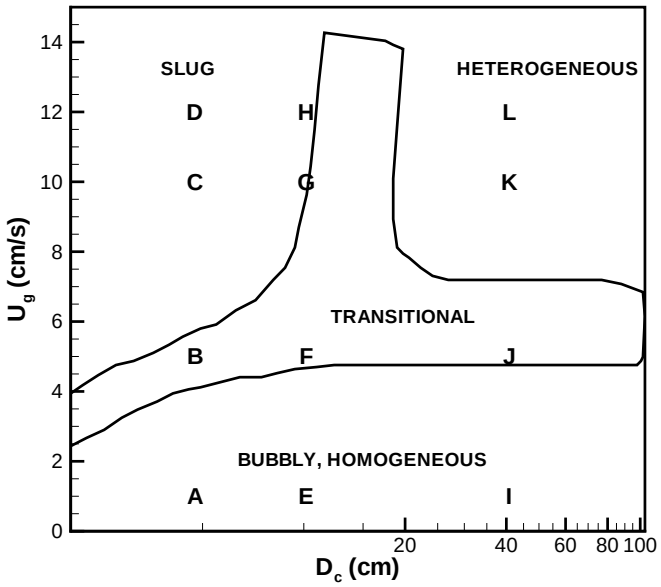


Figure 3.8: Flow regime map based on column diameter and inlet gas velocity [2]. Letters A–L correspond to cases included in this study.

that can coalesce and breakup. Between each regime there is a transition phase where the flow exhibits characteristics of each of the surrounding regimes and is not dominated by any one in particular.

The bubble column diameter was varied for a parametric study to capture different regions of the flow regime map. Keeping the same grid cell size, the column diameter was multiplied by approximately 0.5 and 4, in order examine flows on either side of the transitional region. The simulations were all two-dimensional. Instantaneous gas holdup contours at 90 s are presented in order to determine the type of flow. The instantaneous image will show where bubbles are forming (high gas regions) spatially. The effect of increasing the diameter on the gas holdup pattern at a low inlet gas velocity of $U_g = 1$ cm/s is shown in Figure 3.9, and at a high inlet gas velocity of $U_g = 12$ cm/s in Figure 3.10. For an inlet gas velocity of 1 cm/s (Figure 3.9), all three bubble column sizes are expected to be in the bubbly flow regime. The three cases have about the same gas holdup, as seen by the level of the gas-liquid region and the bubbles show

similar patterns due to the low velocity, indicative of homogeneous flows. For an inlet gas velocity of 12 cm/s (Figure 3.10), the 5 cm column has regions of gas meandering up the column, but for the most part takes up a large portion of the diameter, indicative of bubble slugs. The gas holdup contours for the 40 cm column show more dispersed regions of gas holdup. The gas does not span the full diameter, and there are regions of water in between the bubbles, showing a typical heterogeneous flow. The 10 cm column does seem to have a few places where bubble slugs could form, however it is not definitive. According to the flow regime map (Figure 3.8), this case (H) would be in the slug regime just before transition. The lack of gas holdup near the walls could be error due to the use of a 2D geometry and a single bubble size, both of which will be discussed later. However, this could also be due to a transition happening sooner than reported.

Figure 3.11 shows the effect of inlet gas velocity for a 5 cm column. As the gas velocity increases, bubbles form in larger regions together. These bubbles most likely coalesce due to collisions and form larger bubbles up to the size of the column diameter. Also, the water level is shown to increase from 146 cm to 190 cm, as the inlet gas velocity increases. Figure 3.12 shows the effect of inlet gas velocity for a 40 cm diameter column. In the transitional flow (J), the gas is no longer taking the form of similarly sized bubbles, but is forming into a random bubble motion that appears as a "swirling pattern" in 2D. However, it also does not quite have regions of gas forming together like the heterogeneous flow (K and L). Comparing the 5 and 40 cm diameter columns at the same velocities in the slug (Figure 3.11, C and D) and heterogeneous (Figure 3.12, K and L) regimes, respectively, there is more of a "swirling flow" in the heterogeneous columns with regions of water within the gas as opposed to the gas region spanning the column as in the slug flow cases.

Profiles of gas holdup at a height of 60 cm for the inlet velocity of 12 cm/s, cases D, H, and L, are shown in Figure 3.13. The $x$-location is normalized by the column diameter so that the profiles can be compared. For the instantaneous profiles shown in Figure 3.13(a),

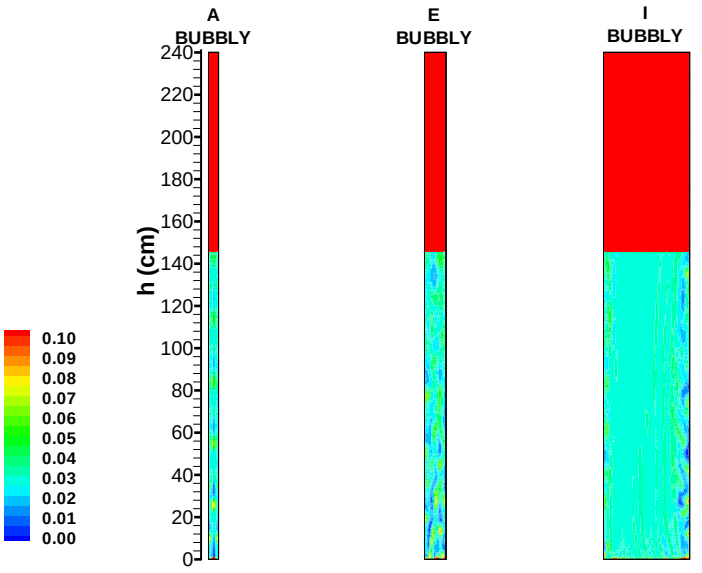


(a) $D_c = 5$ cm (b) $D_c = 10$ cm (c) $D_c = 40$ cm

Figure 3.9: Instantaneous gas holdup contours at 90 s for $U_g = 1$ cm/s showing the flow regime corresponding to Figure 3.8 (A, E, I). Note that the contour levels are lower than that used in later figures.

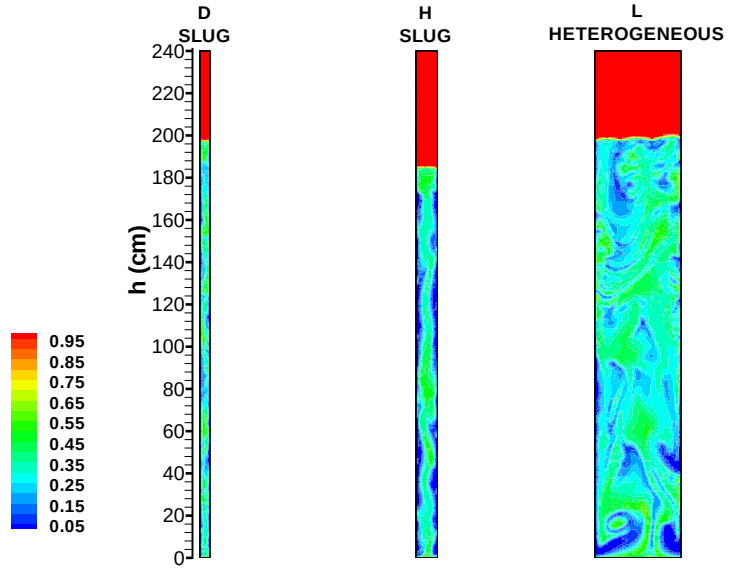


(a) $D_c = 5$ cm (b) $D_c = 10$ cm (c) $D_c = 40$ cm

Figure 3.10: Instantaneous gas holdup contours at 90 s for $U_g = 12$ cm/s showing the flow regime corresponding to Figure 3.8, (D, H, L).

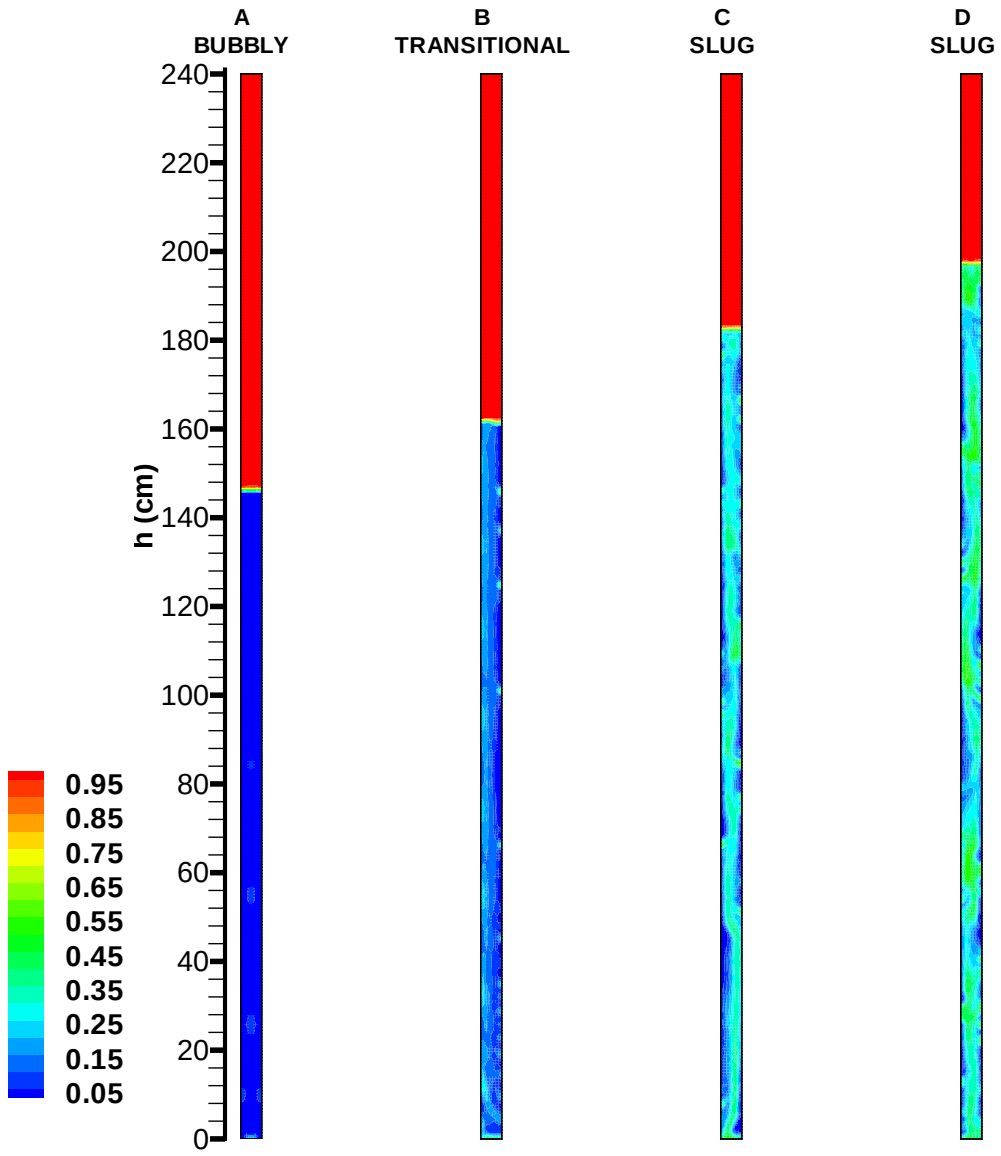


(a) $U_g = 1$ cm/s (b) $U_g = 5$ cm/s (c) $U_g = 10$ cm/s (d) $U_g = 12$ cm/s

Figure 3.11: Instantaneous gas holdup contours at 90 s for $D_c = 5$ cm showing the flow regime corresponding to Figure 3.8, (A, B, C, D).

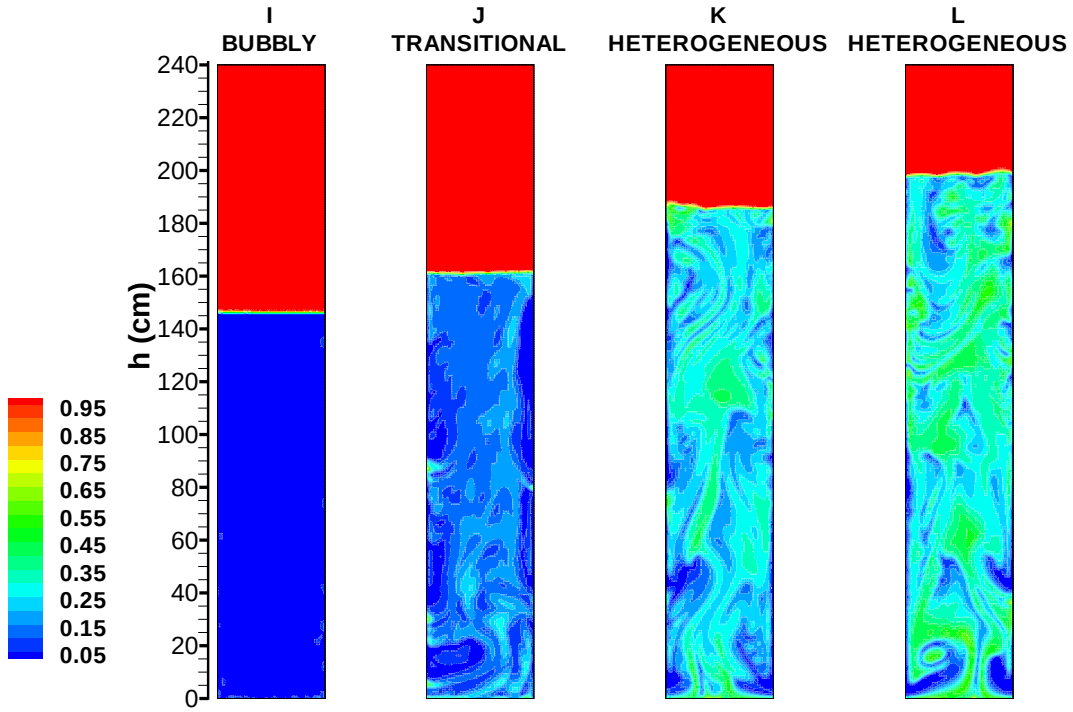


(a) $U_g = 1$ cm/s (b) $U_g = 5$ cm/s (c) $U_g = 10$ cm/s (d) $U_g = 12$ cm/s

Figure 3.12: Instantaneous gas holdup contours at 90 s for $D_c = 40$ cm showing the flow regime corresponding to Figure 3.8, (I, J, K, L).

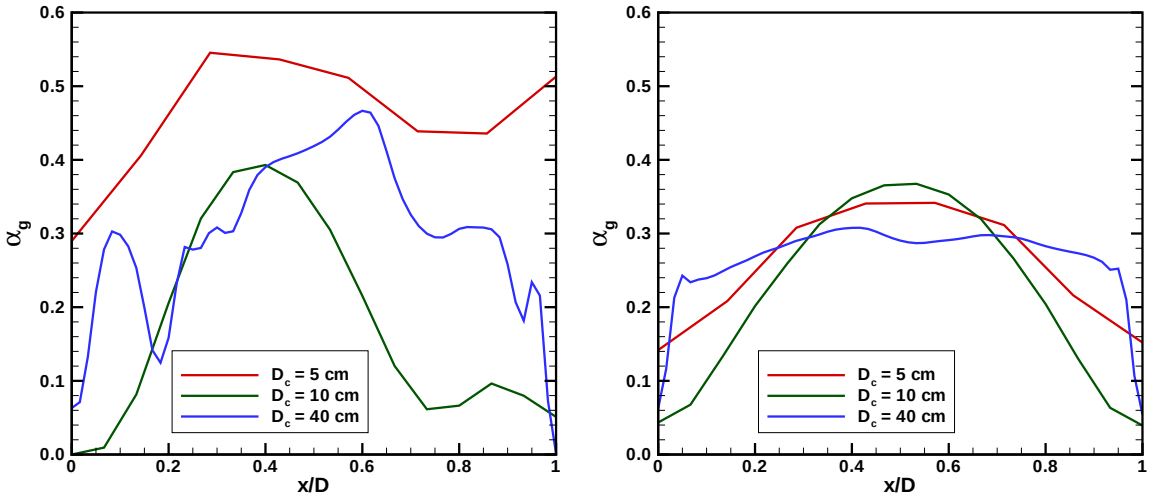


(a) Instantaneous gas holdup (b) Time-averaged gas holdup

Figure 3.13: Gas holdup profiles (a) at 90 s and (b) averaged over 70 s for $U_g = 12$ cm/s.

the 5 cm diameter column (D) is slugging flow evident by the almost uniform region of gas, which is higher than the other cases. The 40 cm diameter column (L) shows more variation and the bubbles are more randomly distributed in the heterogeneous flow. The 10 cm diameter column (H) shows the onset of a transition from slugging flow with a large slug between $x/D = 0.2 - 0.6$. Figure 3.13(b) shows the time-averaged gas holdup profiles for the same three cases. Because the bubbles are more randomly dispersed in the heterogeneous flow ($D_c = 40$ cm, L) than the others, the time-averaging shows that the bubbles move around the width of the column and result in a mostly flat, uniform profile. The transitional flow ($D_c = 10$ cm, H) shows that the large slug bubbles start to break up so there is less gas holdup on the sides of the column and the smaller bubbles mainly flow up the center of the column. The slug flow ($D_c = 5$ cm, D) shows higher gas holdup at the walls than the heterogeneous and transitional flows due to the large diameter bubbles that form spanning the column diameter.

Table 3.3 shows the time-averaged gas holdup for the three column sizes as well as experimental data from Jones [3]. The gas holdup for each case was averaged from $h = 10 - 110$ cm over $20 - 90$ s. At $U_g = 1$ cm/s, the results show all three columns have approximately the same gas holdup, as discussed earlier. However, there is a trend at higher inlet gas velocities. At both $U_g = 10$ and 12 cm/s, each of the three flows are in different flow regimes. The bubbles of the heterogeneous flow ($D_c = 40$ cm) have more mixing than the other flows which results in a higher average gas holdup. The parabolic profile of the transitional flow ($D_c = 10$ cm) results in the lowest gas holdup. In the slug flow ($D_c = 5$ cm), although the bubble slugs are large, which then creates a high local gas holdup, there is more liquid in between them so the average gas holdup is not as high as the heterogeneous flow.

Figure 3.14 shows instantaneous velocity vectors for the 40 cm column at $U_g = 12$ cm/s. The gas velocity 3.14(a) shows a plume originating from the inlet and moving upward with little oscillation throughout the column. Due to drag and the concept of

Table 3.3: Average gas holdup for varying inlet gas velocities using 3 column diameters comparing experiments [3] to simulations.

| | Experiment | Simulations | | |
|---|---|---|---|---|
| $U_g$ | $D_c = 10$ cm | $D_c = 5$ cm | $D_c = 10$ cm | $D_c = 40$ cm |
| 1 cm/s | 0.021 | 0.0275 | 0.0283 | 0.0285 |
| 5 cm/s | 0.145 | 0.1195 | 0.1012 | 0.1166 |
| 10 cm/s | 0.215 | 0.2069 | 0.1955 | 0.2285 |
| 12 cm/s | 0.236 | 0.2499 | 0.2185 | 0.2684 |

added mass, the air carries water with it as it travels upward but the magnitude of the gas velocity decreases as it travels up the column. Near the walls of the column, the gas velocity is low enough that it cannot overcome the density of the water and the water travels downward, carrying some trapped gas bubbles with it, as shown in Figure 3.14(b). In the region of $145 < h < 200$ cm, the gas is still mixed with the liquid but the somewhat parabolic shape of the velocity profile diminishes. The gas flow is mostly upward while the liquid seems to be exactly opposite and tends to move downward because the velocity of the gas is no longer enough to move the heavier liquid and the liquid tries to fill in the spaces below it. Above the water line at $h > 200$, there is only gas which seems to have a mostly upward but somewhat recirculating pattern.

## 3.3 Comparison to Experimental Results

Jones [3] performed experiments using a 10.2 cm bubble column riser, and varying the inlet gas velocities from 0.5 to 20 cm/s and measuring gas holdup. The column height is 240 cm with static liquid height of 142 cm. It was observed that gas holdup increased with increasing gas velocity. Both two-dimensional (2D) and three-dimensional (3D) simulations will be validated with the experiments. The column is modeled with no-slip walls and an inlet and outlet at the bottom and top. The inlet has a specified gas velocity normal to the opening. The outlet pressure is 0 Pa gage and the gas is allowed to flow out of the top as needed. Initially, the 240 cm column height is filled with static

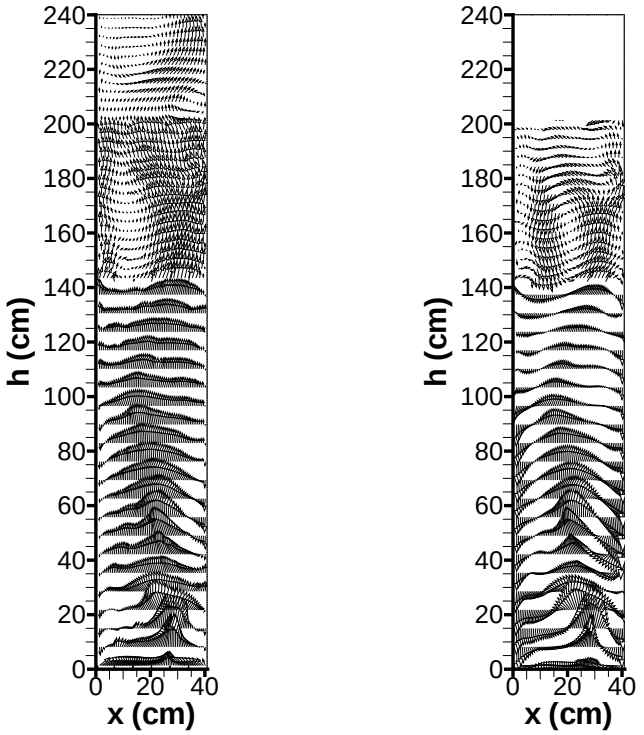


(a) gas velocity (b) liquid velocity

Figure 3.14: Instantaneous velocity vectors for $D_c = 40$ cm at $U_g = 12$ cm/s for the (a) gas phase and (b) liquid phase.

water up to 142 cm.

### 3.3.1 2D Simulations

As mentioned in the Introduction, the entire bubble population may not be a single size formed from the inlet at the sparger due to growth, coalescence, and breakup. In an attempt to simulate that higher gas velocities will result in larger bubbles, cases were run using different bubble diameters for different inlet gas velocities. From 1 to 15 cm/s, a bubble diameter of 0.4 cm was used; at 15 cm/s a bubble diameter of 0.5 cm was also used; and at 20 cm/s, 0.5, 0.6, 0.7, and 0.8 cm was used. The 10.2 $\times$ 240 cm 2D grid is composed of 15 $\times$ 353 square cells.

The gas holdup was averaged in the domain from $h = 10 - 110$ cm, over $20 - 90$ s for each case. Figure 3.15 compares the gas holdup from Jones [3] to the numerical

simulations and shows that the simulations follow a similar trend as the experiments. The limitation of neglecting growth, breakage, and coalescence of bubbles prevents the simulations from accurately predicting the amount of gas holdup, however most of the data falls within the range of experimental uncertainty. The results differ the most in the transitional region of 5 to 10 cm/s for the 10 cm diameter column. The bubbles may be mixed in size; for example, a few large bubbles may have smaller bubbles in between that occupy more volume than just one bubble size, which the simulations do not model. There is no agreed upon method for determining the correct effective bubble diameter [5, 25] but it is necessary to choose the appropriate size for the simulation conditions. In the cases where there were multiple effective bubble diameters tested, the average gas holdup decreases as bubble size increases. As the inlet gas velocity increases, it is necessary to increase the size of the effective bubble diameter. As determined in the grid resolution study, decreasing the time step for situations where the bubble diameter exceeds the cell size helps to obtain stable and converged solutions. An unconverged solution causes a violation of conservation of mass. For an inlet gas velocity $U_g = 20$ cm/s, bubble diameters of $d_b = 0.5$ cm, 0.6 cm, 0.7 cm, and 0.8 cm were used. The time step for $d_b = 0.5$ cm and 0.6 cm was 0.005 s and for $d_b = 0.7$ cm and 0.8 cm was 0.001 s. The gas holdup for the three larger bubble diameters, $d_b = 0.6$, 0.7, and 0.8 cm, fall within 0.006 of each other and are within the experimental uncertainty. Increasing the bubble diameter while decreasing the time step does not significantly improve the results and not enough information is gained to be worth the extra CPU time required. There seems to be some limitations when using a two-dimensional model so similar cases are tested using a three-dimensional domain.

### 3.3.2 3D Simulations

An unstructured grid in the horizontal plane is used, as shown in Figure 3.16, keeping within an approximate cell size of 0.68 cm per side. The use of an unstructured grid allows

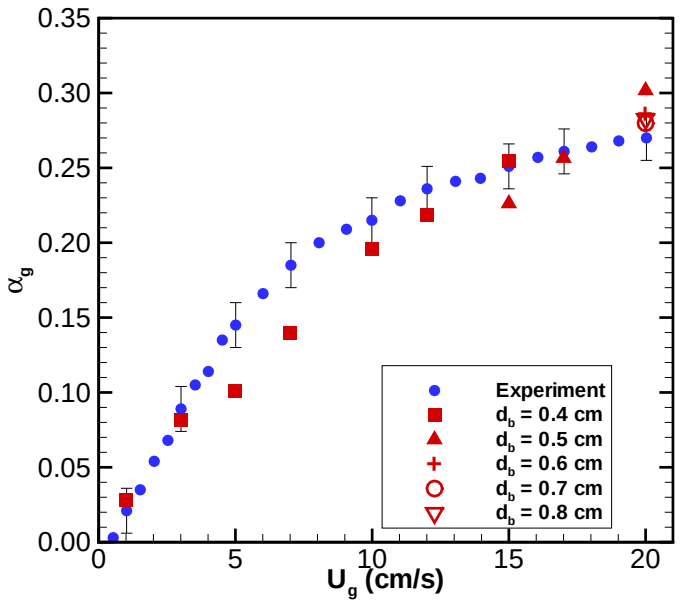


Figure 3.15: Average gas holdup for inlet gas velocities comparing experiments [3] with 2D simulations using different bubble diameters.

for the cells to have a fairly consistent size. From the 2D simulations, it was found that a bubble size of 0.4 cm works well for the range of $U_g = 5 - 15$ cm/s.

The average gas holdup from $20-90$ s over $h = 10-110$ cm is presented in Figure 3.17. For the lowest velocity of 5 cm/s, the resulting average gas holdup differs slightly less to the experimental data than the 2D results. However, at higher velocities the 3D predictions for average gas holdup are $27-31\%$ lower than the experiments, whereas the 2D model predictions fall within experimental error. This is not as expected as the 3D column is a more correct geometrical representation of the experimental column. From the 2D results it was noted that a larger bubble size at the same velocity results in lower overall gas holdup. Therefore using a bubble size of 0.5 or 0.6 cm as before should result in larger differences. However, once again mixing of bubble sizes which the simulations do not model may allow for larger values of gas holdup due to smaller bubbles being able to fill in "gaps" created by larger bubbles.

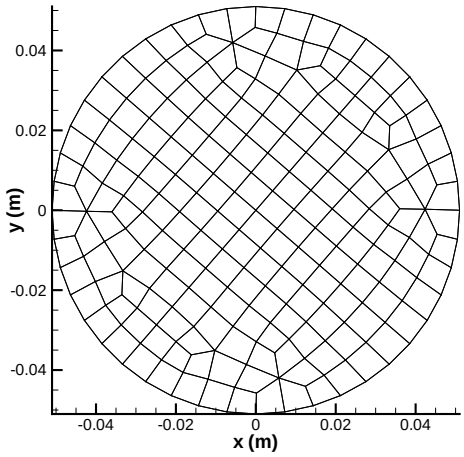


Figure 3.16: Unstructured grid for the 3D bubble column

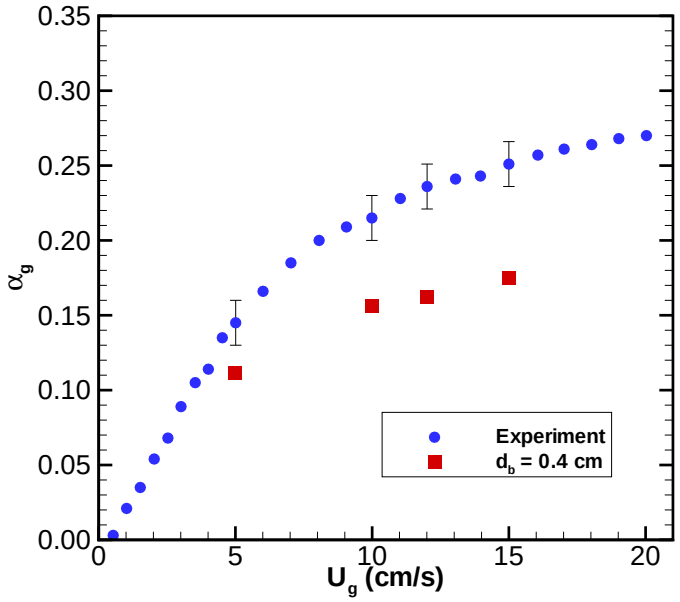


Figure 3.17: Average gas holdup for inlet gas velocities comparing experiments [3] with 3D simulations.

# Chapter 4. Airlift Reactor

## 4.1 Problem Description

An airlift reactor differs from a bubble column in that the addition of a downcomer allows for more circulation and mixing through the riser. The first part of this chapter will compare the gas holdup and velocity of the airlift reactor to the bubble column to see how the mixing is affected. Next, three-dimensional models will be compared to the two-dimensional models. The effect of modeling the effective bubble diameter will also be examined.

Jones [3] performed experiments using an external airlift reactor with a riser diameter of $D_r = 10.2$ cm and a downcomer diameter of $D_d = 2.5$ cm. The riser has height $H_r = 240$ cm and static liquid height $h_0 = 142$ cm, as defined in Figure 4.1. The geometry will serve as a basis for the simulations and discussion. Varying the inlet gas velocity from 0.5 to 20 cm/s, gas holdup in the riser and downcomer and liquid velocity in the downcomer were measured. For the simulations presented in this chapter, the airlift reactor is modeled with no-slip walls, an inlet at the bottom of the riser, and outlets at the top of the riser and downcomer. The inlet has a specified gas velocity normal to the opening. The outlet is 0 Pa gage pressure and the gas is allowed to flow out of the top as needed.

The cell size of the two-dimensional geometry was modified slightly from the bubble column (Chapter 3) from 0.68 cm to 0.64 cm to account for the narrow downcomer. The smaller cell size introduces difficulty in modeling an effective bubble diameter of 0.6 cm or larger for the airlift reactor. For $U_g = 1$ cm/s to 15 cm/s, an effective bubble diameter

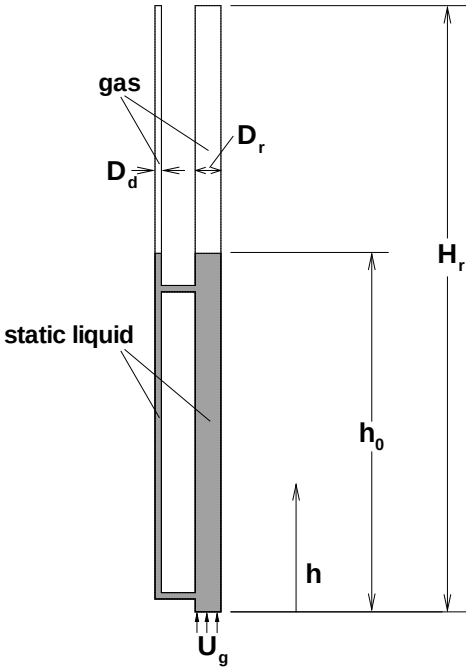


Figure 4.1: Schematic and variable definitions for an airlift reactor.

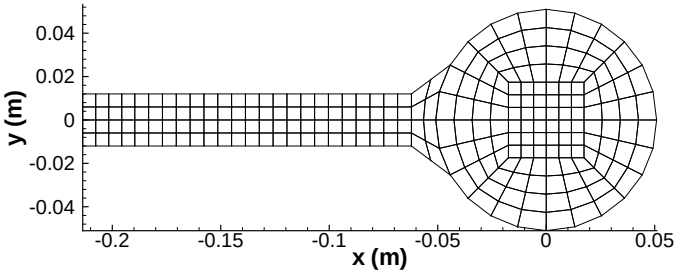


Figure 4.2: Top view of the grid for the 3D airlift reactor.

$d_b = 0.4$ cm was used and for $U_g = 15$ and 20 cm/s, $d_b = 0.5$ cm. The three-dimensional geometry is composed of a cylindrical riser with $D_r = 10.2$ cm and square cross-section downcomer and connectors with $D_d = 2.4$ cm, which is the hydraulic diameter necessary to conserve the volumetric flow. The riser has an unstructured grid with an approximate cell size of 0.64 cm in the horizontal plane and a uniform cell height of 0.64 cm. The downcomer and connectors have a structured grid with the cell size in the $x$- and $y$-directions of 0.6 cm, as shown in Figure 4.2. The convergence criteria for the 2D case was set to $10^{-4}$ with 200 maximum pseudo-iterations per time step. The convergence

Table 4.1: CPU requirements for 2D and 3D ALR simulations.

| | 2D | 3D |
|---|---|---|
| CPU (h) | 3.9 | 297.8 |
| # time steps | 9,000 | 9,000 |
| $\Delta t$ (s) | 0.005 | 0.005 |
| # cells | 7,716 | 56,372 |
| CPU/timestep/cell ($\mu s$) | 203 | 2,113 |

criteria for the 3D case was increased to $10^{-3}$ due to the large CPU time required to reach the convergence of $10^{-4}$ and used 100 maximum pseudo-iterations per time step. Both the 2D and 3D cases used a time step of $\Delta t = 0.005$ s. The 3D case was started with $\Delta t = 0.0005$ s due to instability from the initial quiescent flow and simulated for 5 s before increasing the time step to 0.005 s. The CPU requirements for a typical 2D and 3D case are shown in Table 4.1. The 3D case uses 10 times more CPU/timestep/cell than the 2D case. For this reason, the 2D cases were able to simulate 90 s of time and the data presented is averaged over 70 s while the 3D cases were simulated for 60 s and the data averaged over 45 s.

## 4.2 Comparison to Bubble Column

Time-averaged gas holdup contours for the two-dimensional airlift reactor (ALR) and bubble column (BC) at $U_g = 10$, 15 and 20 cm/s are shown in Figures 4.3, 4.4, and 4.5. The gas holdup in the airlift reactor has a back and forth pattern near the bottom of the riser resembling a regular oscillation, which is absent in the bubble column. At the lower connector, the water flows into the riser from the downcomer which pushes the gas inflow to the opposite side of the riser. For the $U_g = 10$ cm/s case (a), the gas oscillations reduce at approximately 30 cm above the riser inlet and forms a straight path until it reaches the upper connector. In addition, the gas stream tends to meander toward the riser wall between the connectors. As the inlet gas velocity increases to $U_g = 15$ cm/s (a), the flow continues to oscillate up to 115 cm before being disturbed again by the influence

of the upper connector. At $U_g = 20$ cm/s (a), the high inlet velocity causes the flow to become more uniform above $h = 40$ cm and becomes stable due to the column walls. In all cases of the airlift reactor, there is also a similar pattern above the upper connector but it is not as pronounced because the gas completely leaves the top of the free surface in a short distance after the connector. In contrast to the airlift reactor, the bubble column has no recirculation with only the bottom inlet present and therefore the gas is free to move upward and equally fill the column. As was shown in the instantaneous contours of Figure 3.10 (Chapter 3), the gas does not always fill the entire column and has an irregular pattern. The time-averaged data of Figures 4.3 - 4.5 shows that the gas occupies more area of the column in the bubble column than in the airlift reactor. In each case, the average level of the gas-liquid flow is higher in the bubble column than the airlift reactor due to the increase in gas holdup of the bubble column. The difference ($\Delta h$) increases with increasing inlet gas velocity with $\Delta h = 15$ cm for $U_g = 10$ cm/s and $\Delta h = 30$ cm for $U_g = 20$ cm/s.

In comparison to the 2D ALR simulations, contours of time-averaged gas holdup at the center plane of the airlift reactor for 3D simulations are also shown in Figures 4.3, 4.4, and 4.5. The 3D simulations do not show as much oscillation at the bottom of the riser. For $U_g = 10$ cm/s (Figure 4.3(b)), there is a small amount of oscillations below $h = 20$ cm and the flow concentrates itself toward the center of the column rather than closer to the connectors and takes up a wider region of the column than the 2D case. At higher velocities ($U_g = 15, 20$ cm/s), the gas spans most of the diameter of the riser because in 3D it can also expand azimuthally. Figure 4.6 shows contours of time-averaged gas holdup of the $U_g = 10$ and 20 cm/s 3D simulations in the horizontal planes at the upper connector, $h = 128$ cm, middle of the initial static liquid region, $h = 61$ cm, and lower connector, $h = 6$ cm. The gas holdup region in the cross-section at $h = 128$ cm is relatively uniform with higher regions of liquid along the circumference of the riser. There are also bubbles flowing into the connector, which manifest as a uniformly distributed

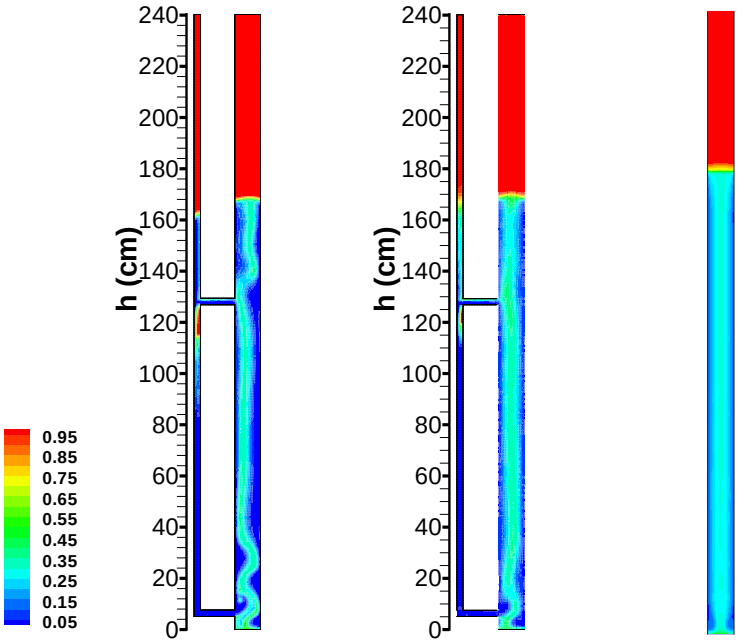


(a) 2D ALR (b) 3D ALR (c) 2D BC

Figure 4.3: Time-averaged gas holdup contours for $U_g = 10$ cm/s for the (a) 2D airlift reactor, (b) 3D airlift reactor, and (c) 2D bubble column simulations.

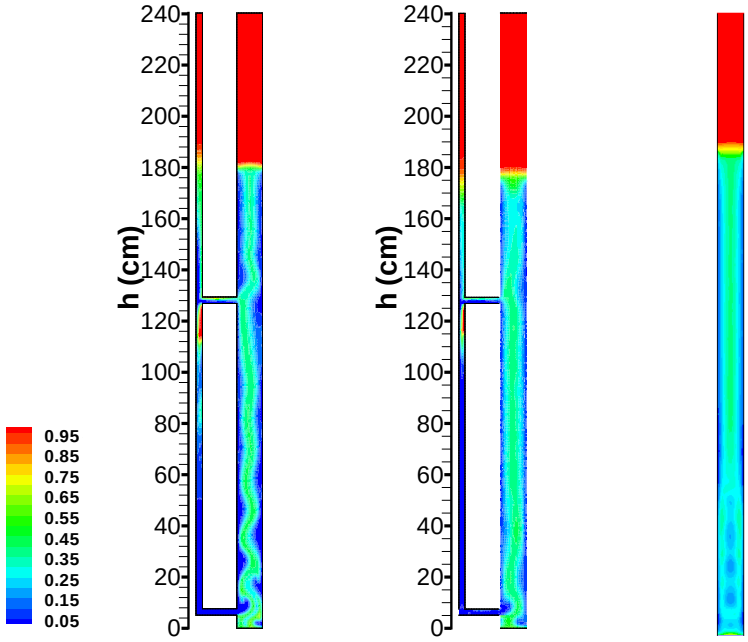


(a) 2D ALR (b) 3D ALR (c) 2D BC

Figure 4.4: Time-averaged gas holdup contours for $U_g = 15$ cm/s for the (a) 2D airlift reactor, (b) 3D airlift reactor, and (c) 2D bubble column simulations.

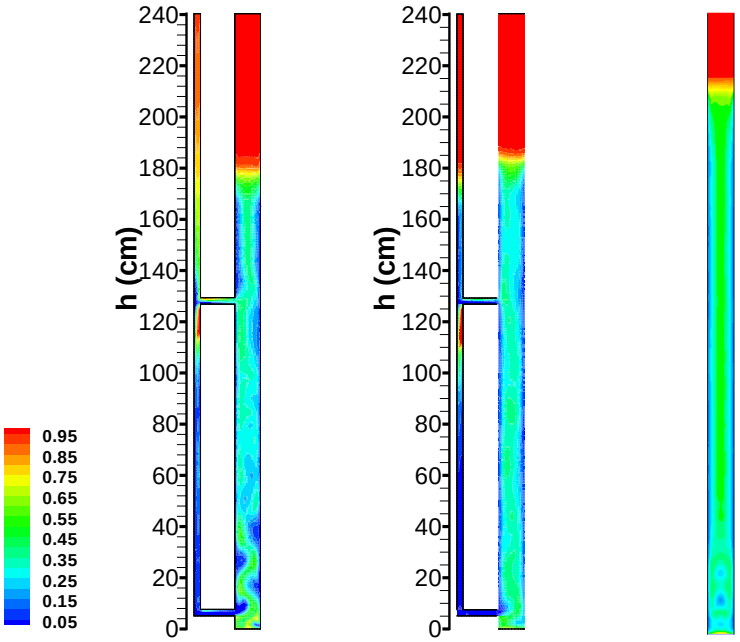


(a) 2D ALR (b) 3D ALR (c) 2D BC

Figure 4.5: Time-averaged gas holdup contours for $U_g = 20$ cm/s for the (a) 2D airlift reactor, (b) 3D airlift reactor, and (c) 2D bubble column simulations.

region. The region of gas in the riser is larger for $U_g = 20$ cm/s than $U_g = 10$ cm/s and Figure 4.3 shows that gas occupies the upper half of the connector and liquid flows through the lower half. At $h = 61$ cm, the gas holdup across the riser increases as the inlet gas velocity increases from 10 cm/s to 20 cm/s. The cross-section through the lower connector for $U_g = 10$ cm/s shows that the gas region is very nonuniform due to the liquid flow out of the connector. The higher inlet gas velocity of $U_g = 20$ cm/s increases the gas holdup and therefore occupies most of the riser; however the large amount of liquid flow from the lower connector is still shown.

Profiles of average gas holdup ($\alpha_g$), gas velocity ($V_g$), and liquid velocity ($V_l$) at different heights along the airlift reactor riser and bubble column are shown in Figures 4.7, 4.8, 4.9 for $U_g = 10$, 15, and 20 cm/s, respectively. The first column in each figure are the 2D airlift reactor results, the middle column are the 3D airlift reactor results, and the last column are the 2D bubble column results. The upper row in each figure is the

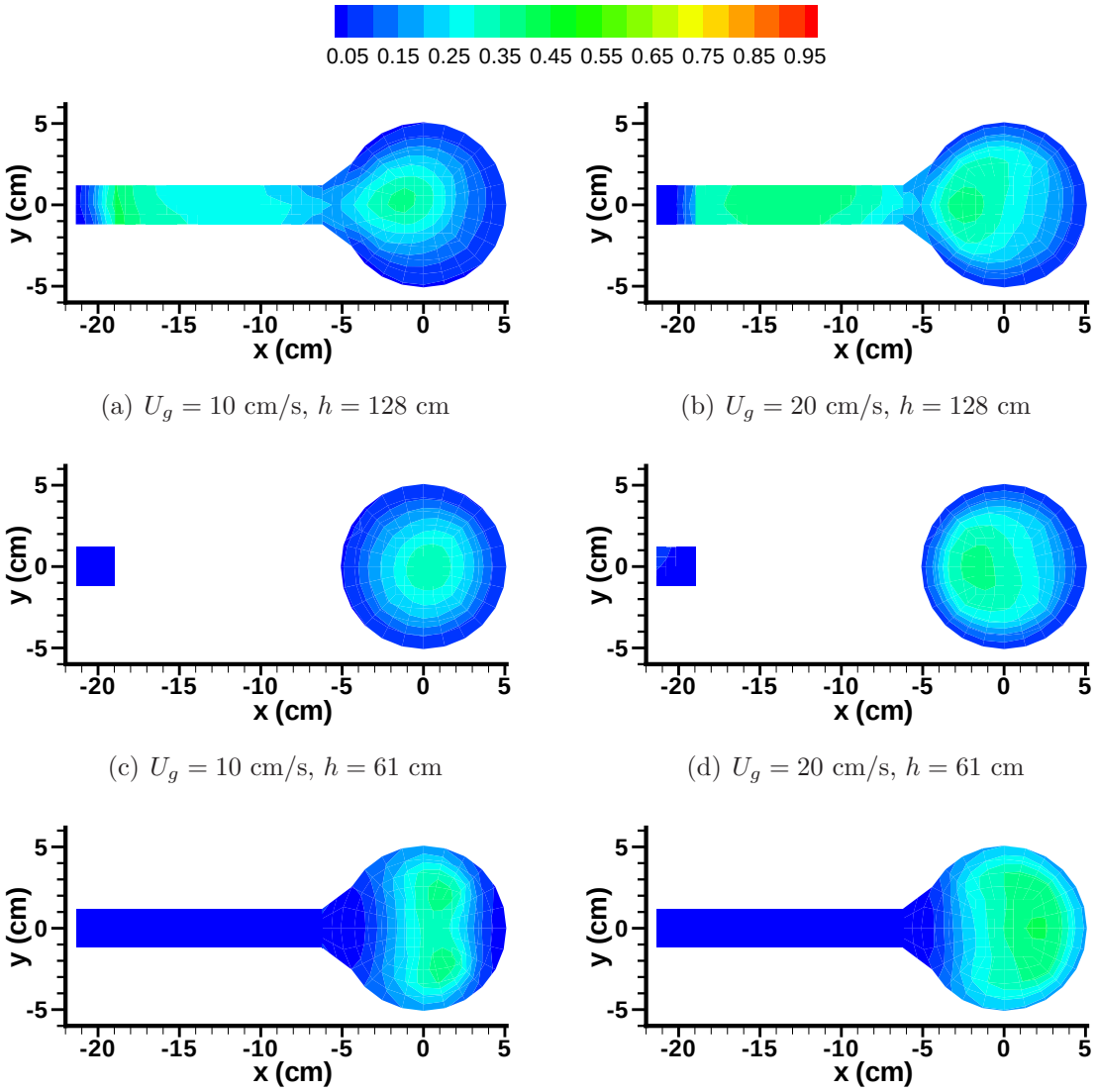


(a) $U_g = 10$ cm/s, $h = 128$ cm

(b) $U_g = 20$ cm/s, $h = 128$ cm

(c) $U_g = 10$ cm/s, $h = 61$ cm

(d) $U_g = 20$ cm/s, $h = 61$ cm

(e) $U_g = 10$ cm/s, $h = 6$ cm

(f) $U_g = 20$ cm/s, $h = 6$ cm

Figure 4.6: Time-averaged gas holdup contours for horizontal planes of 3D airlift reactor simulations.

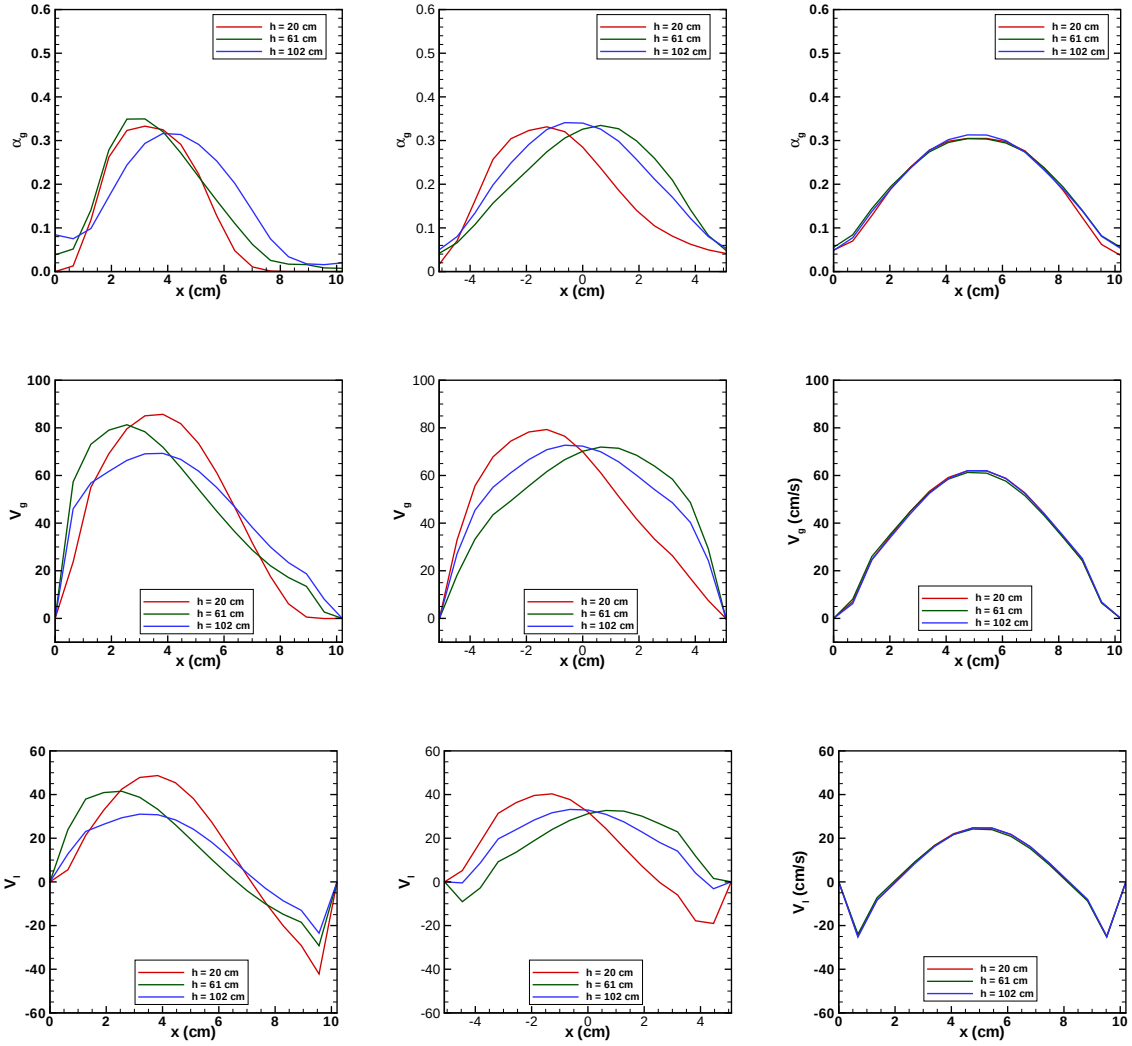


(a) 2D ALR (b) 3D ALR (c) 2D BC

Figure 4.7: Time-averaged gas holdup, gas velocity, and liquid velocity profiles for $U_g$ = 10 cm/s at $h$ = 20, 61, and 102 cm for the (a) 2D airlift reactor, (b) 3D airlift reactor, and (c) 2D bubble column simulations.

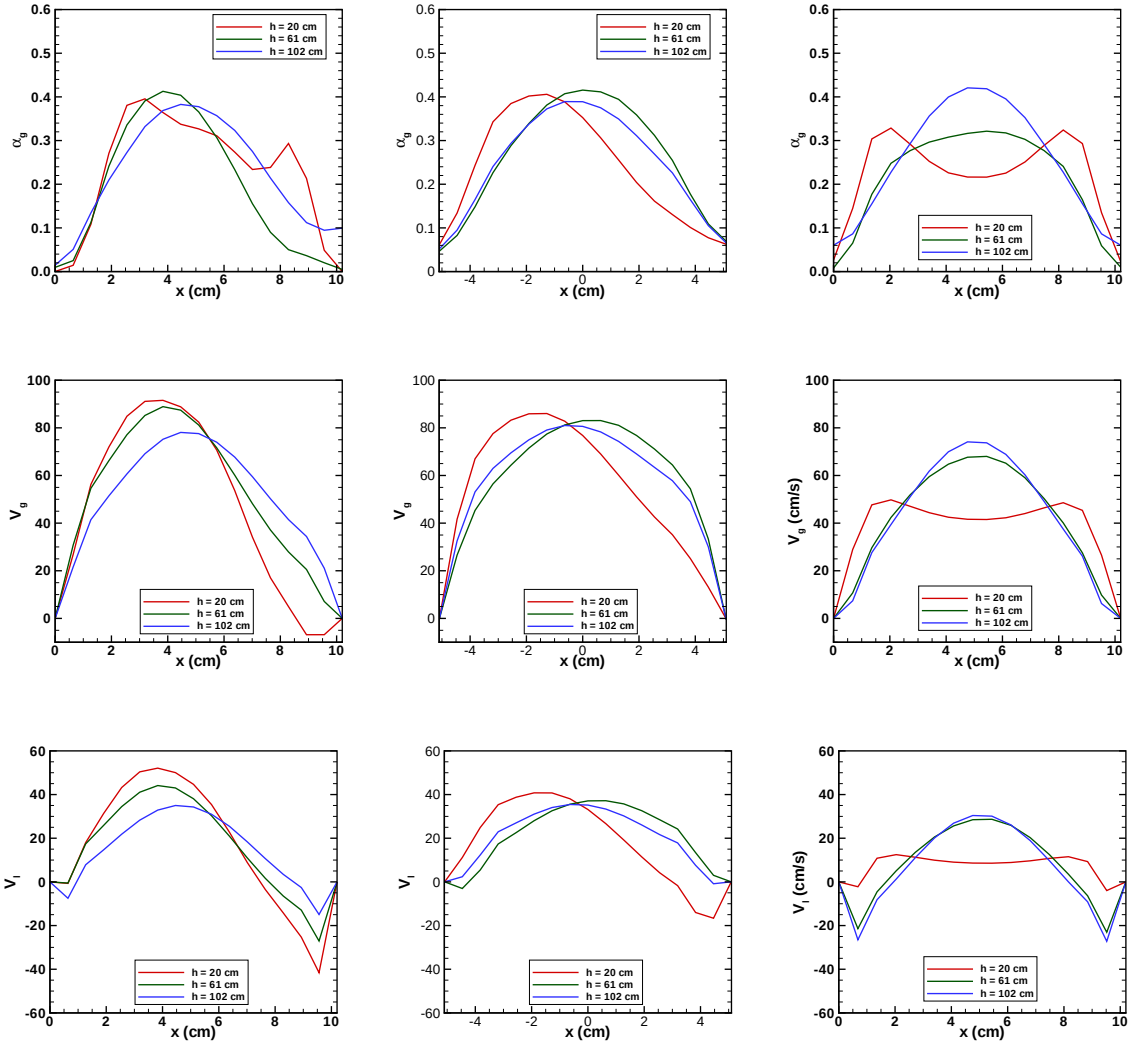


(a) 2D ALR (b) 3D ALR (c) 2D BC

Figure 4.8: Time-averaged gas holdup, gas velocity, and liquid velocity profiles for $U_g$ = 15 cm/s at $h$ = 20, 61, and 102 cm for the (a) 2D airlift reactor, (b) 3D airlift reactor, and (c) 2D bubble column simulations.

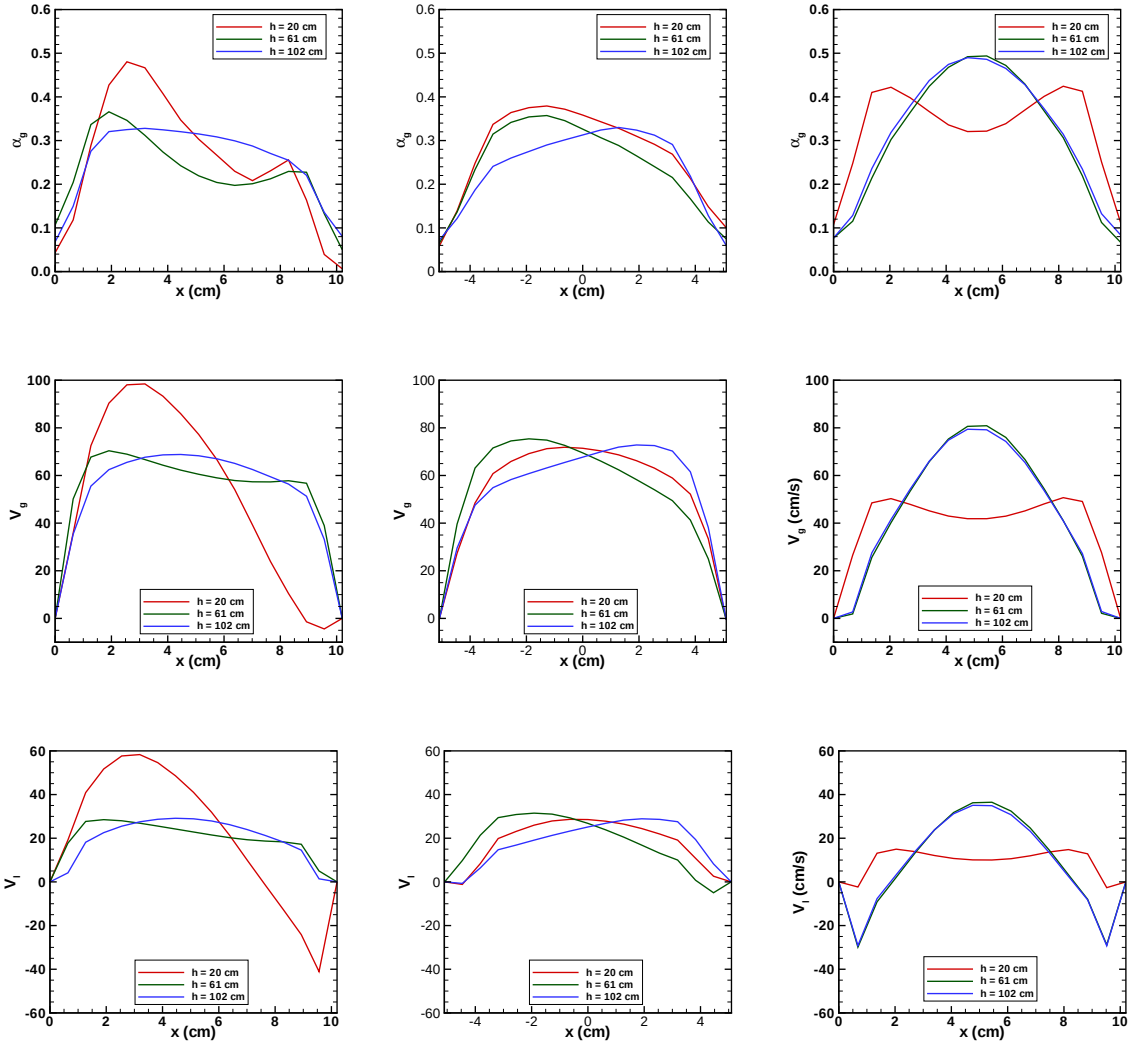


(a) 2D ALR (b) 3D ALR (c) 2D BC

Figure 4.9: Time-averaged gas holdup, gas velocity, and liquid velocity profiles for $U_g$ = 20 cm/s at $h$ = 20, 61, and 102 cm for the (a) 2D airlift reactor, (b) 3D airlift reactor, and (c) 2D bubble column simulations.

gas holdup, the middle row is the gas velocity, and the bottom row is the liquid velocity. The 3D airlift reactor profiles are taken from the center-plane of the riser. All cases of the 2D airlift reactor show the maximum velocity and gas holdup off-center of the riser due to the connectors and downcomer, while the bubble column profiles are symmetric in all three variables. The maximum gas and liquid velocities of the 2D airlift reactor decrease as column height increases and the profiles never become independent of column height, irrespective of inlet velocity, due to the enhanced mixing within the reactor. The 3D airlift reactor gas and liquid velocities do not show the same trend for all $U_g$. For $U_g = 10$ cm/s (Figure 4.7(b)), the maximum velocity is highest at $h = 20$ cm and the $h = 61$ and 102 cm profiles have similar maxima. For $U_g = 15$ cm/s (Figure 4.8(b)), the gas and liquid velocities decrease as column height increases and the profiles become more parabolic after 20 cm but never independent of column height. For $U_g = 20$ cm/s (Figure 4.9(b)) the maximum velocities are lowest at $h = 20$ cm and then increase as the flow is influenced by the connector more than the low inlet velocity, shown by the off-centered profiles at $h = 61$ and 102 cm. In contrast to the airlift reactor, the bubble column velocity profiles at $U_g = 10$ cm/s (Figure 4.7(c)) collapse at all heights shown. For higher inlet velocities, the gas and liquid velocities are relatively uniform near the bottom and collapse onto parabolic curves higher up the column. For all inlet velocity cases, the maximum gas holdup, gas velocity, and liquid velocity are similar in magnitude between the 2D and 3D airlift reactor simulations. As shown in Tables 4.2, 4.3, and 4.4, the gas holdup in the airlift reactor is lower than in the bubble column at comparable height and inlet velocity, however the gas and liquid velocities shown are greater in the airlift reactor than the bubble column. This shows that the velocity of the flow in the riser can be increased by using an airlift reactor without increasing the inlet velocity, which will enhance the mixing.

Time-averaged velocity vectors for each phase are shown superimposed onto the respective volume fraction contours for the 2D simulations in Figures 4.11 and 4.10. The

Table 4.2: Average gas holdup for the 2D ALR and BC simulations.

| | $U_g = 10$ cm/s | | $U_g = 15$ cm/s | | $U_g = 20$ cm/s | |
|---|---|---|---|---|---|---|
| $h$ | ALR | BC | ALR | BC | ALR | BC |
| 20 cm | 0.1299 | 0.2025 | 0.2383 | 0.2345 | 0.2662 | 0.342 |
| 61 cm | 0.1504 | 0.2077 | 0.1993 | 0.2254 | 0.2365 | 0.3235 |
| 102 cm | 0.1622 | 0.2074 | 0.2325 | 0.2617 | 0.2632 | 0.3318 |

Table 4.3: Average gas velocity (cm/s) for the 2D ALR and BC simulations.

| | $U_g = 10$ cm/s | | $U_g = 15$ cm/s | | $U_g = 20$ cm/s | |
|---|---|---|---|---|---|---|
| $h$ | ALR | BC | ALR | BC | ALR | BC |
| 20 cm | 44.84 | 37.89 | 47.56 | 39.77 | 52.54 | 40.58 |
| 61 cm | 45.25 | 37.67 | 52.76 | 43.10 | 56.00 | 46.01 |
| 102 cm | 44.88 | 37.74 | 51.47 | 43.55 | 55.45 | 45.99 |

Table 4.4: Average liquid velocity (cm/s) for the 2D ALR and BC simulations.

| | $U_g = 10$ cm/s | | $U_g = 15$ cm/s | | $U_g = 20$ cm/s | |
|---|---|---|---|---|---|---|
| $h$ | ALR | BC | ALR | BC | ALR | BC |
| 20 cm | 14.2 | 5.17 | 17 | 7.65 | 22.27 | 9.59 |
| 61 cm | 12.38 | 5.01 | 16.33 | 8.59 | 20.11 | 9.53 |
| 102 cm | 11.97 | 5.09 | 14.93 | 6.91 | 19.89 | 9.2 |

average volume fraction of each phase follows the pattern of the velocity. The gas-liquid flow reaches a maximum height, above which only gas is present. First analyzing the water flow patterns for $U_g = 5$ cm/s (Figure 4.10(a)), shows that the flow stops oscillating at about $h = 25$ cm and the water occupies the side of the riser opposite of the connectors. Thus, the gas velocity (Figure 4.11(a)) shows that the bubbles rise along side the wall closest to the connectors. Above the connectors, the water is unable to sustain the upward movement and creates a recirculation region that spans most of the riser. The water flowing closest to the wall eventually moves downward. As the inlet gas velocity is increased to $U_g = 10$ cm/s, more bubbles move upward and begin to fill the riser (Figure 4.11(b)). The flow above the upper connector is slightly off-center and the liquid forms two small recirculating regions on either side of the gas flow. Further increasing the gas inlet velocity (Figures 4.11(c), (d)), increases the bubble oscillations as the gas moves upward, and the gas fills more of the riser. Although less evident, the liquid forms recirculation regions above the upper connector (Figures 4.10(c), (d)) and

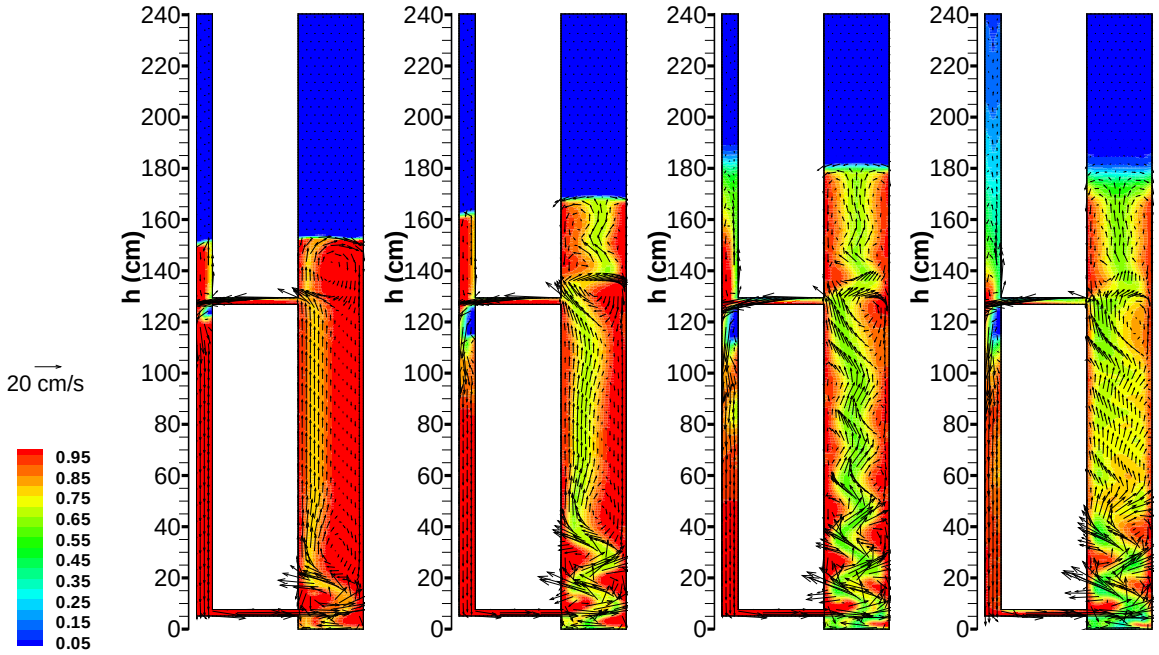


(a) 5 cm/s (b) 10 cm/s (c) 15 cm/s (d) 20 cm/s

Figure 4.10: Time-averaged liquid velocity vectors superimposed onto liquid volume fraction contours. Geometry not to scale.

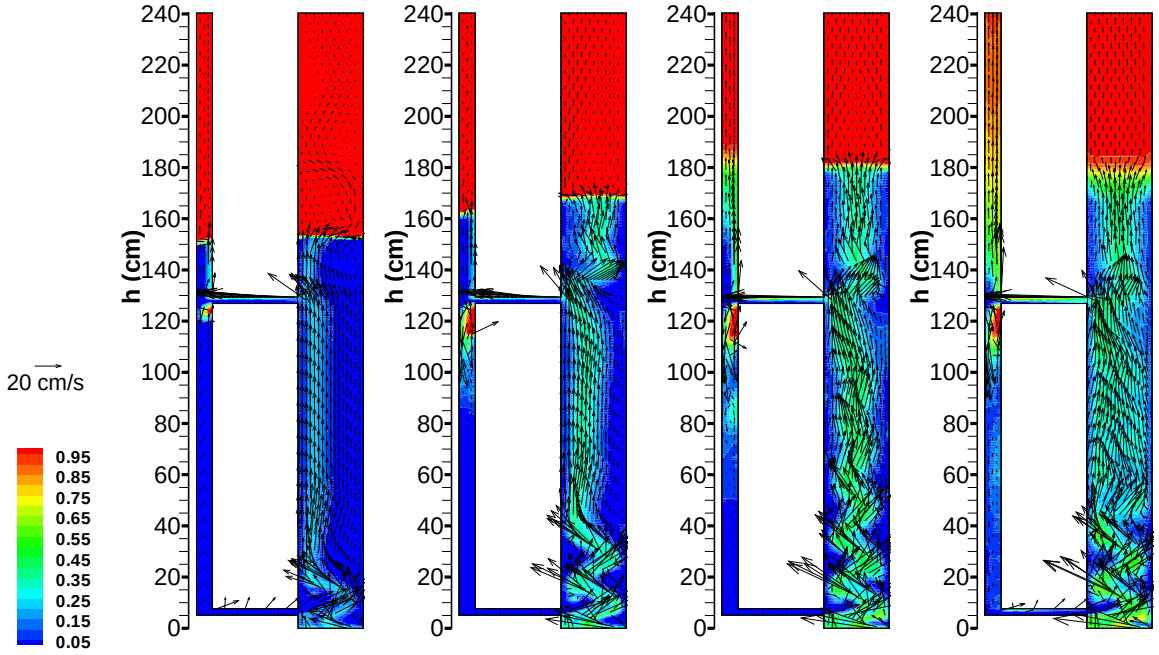


(a) 5 cm/s (b) 10 cm/s (c) 15 cm/s (d) 20 cm/s

Figure 4.11: Time-averaged gas velocity vectors superimposed onto gas holdup contours. Geometry not to scale.

descends along the walls.

The gas-liquid flow splits once it enters the downcomer from the upper connector. The gas has a higher velocity above the connector than below and the liquid that moves downward is faster than the gas in the same region below the upper connector. All inlet gas velocity cases show a region of high gas holdup forming a large bubble in the downcomer below the upper connector. The liquid moving down the downcomer carries some gas with it but the gas overcomes the downward momentum and starts to move upward. The gas then gets trapped below $h = 127$ cm by the cross flow from the connector to create this bubble. The same phenomenon was observed by Jones [3].

As a further comparison of the results, data from Jones [3] are presented to determine how well the CFD predictions match with the experiments. The gas holdup in both the riser and downcomer was averaged from $h = 10-110$ cm over 70 s for the two-dimensional simulations and over 45 s for the three-dimensional simulations. Figure 4.12 compares the gas holdup from Jones [3] to the two- and three-dimensional simulations. Except for $U_g = 1$ cm/s, the 2D simulation results for gas holdup in the riser are lower than the experimental and 3D results. The 2D simulations also significantly underpredict the downcomer gas holdup for $U_g = 5$ and 10 cm/s, while the results for $U_g = 15$ cm/s are within experimental error for both $d_b = 0.4$ and 0.5 cm and the result for $U_g = 20$ cm/s is overpredicted from the experimental gas holdup. As the inlet gas velocity increases, it is necessary to increase the effective bubble diameter for more accurate predictions. The larger effective bubble diameter for $U_g = 15$ cm/s predicts a slightly higher gas holdup than the smaller effective bubble diameter. The 3D simulations give better predictions than the 2D simulations for the riser gas holdup, with all inlet gas velocities tested falling within experimental error. In the downcomer, all 3D simulations except for $U_g = 20$ cm/s significantly underpredict the gas holdup. The 3D FLUENT simulations are useful for predicting gas holdup in the riser of an airlift reactor but not the downcomer, however the riser is where most of the gas-liquid interactions take place in an airlift reactor and

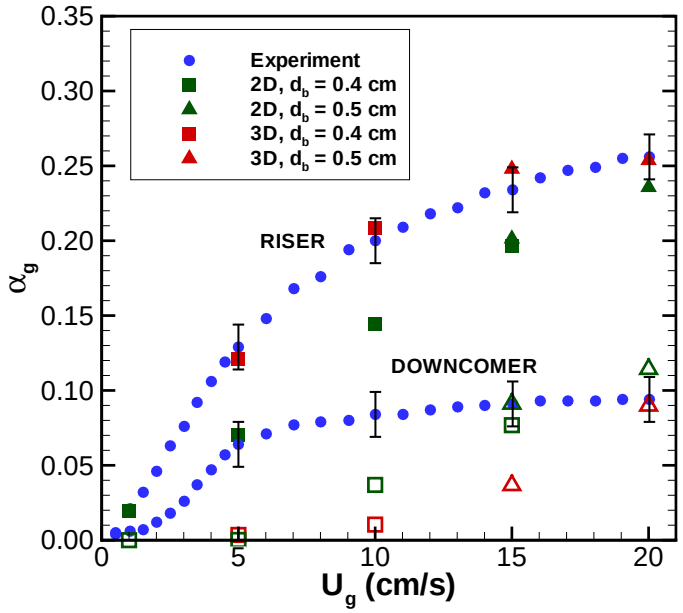


Figure 4.12: Average gas holdup comparing experiments [3] with 2D and 3D simulations using two different bubble diameters.

therefore the more important feature of the two.

# Chapter 5. Conclusions and Future Work

## 5.1 Conclusions

Bubble columns and airlift reactors are useful in the chemical, biotechnology, and pharmaceutical industries. An airlift reactor is advantageous over bubble columns because they can improve mixing without the added stress from high velocities. As a means to better understand the hydrodynamics, it is advantageous to numerically model an air-water flow in these reactors to analyze the mixing characteristics of each configuration.

In these simulations, an Eulerian-Eulerian approach was used to model air as the dispersed phase within a continuous phase of water using the commercial software FLUENT. The Schiller-Naumann drag model was employed along with virtual mass and the standard $k - \epsilon$ turbulence model. The equations were discretized using the QUICK scheme and solved with the SIMPLE coupling algorithm. A single effective bubble diameter was specified for each case studied and depended on the inlet gas velocity specified.

The flow regimes of a standard bubble column were investigated by varying the column diameter and the inlet gas velocity using two-dimensional simulations. The typical characteristics of a homogeneous, slug, and heterogeneous flow were shown using contours of gas holdup. The gas holdup patterns were similar for the low velocity cases of each column size in the homogeneous regime. The slug flow regime cases of the 5 and 10 cm diameter columns showed large regions of bubble clusters that would form bubble slugs. The 40 cm diameter column cases showed large bubble clusters forming but the larger

diameter caused more breakup and therefore a heterogeneous flow was observed, which showed a large amount of mixing. The flow regime map discussion was only applied to bubble columns and it was not known whether the transitions between regimes occur at the same parameters in an airlift reactor.

The average gas holdup in a 10.2 cm diameter bubble column was calculated for two- and three-dimensional simulations and was shown to increase with increasing inlet gas velocity, which was the same trend reported by Jones [3]. The two-dimensional simulations performed better than the three-dimensional simulations with most of the two-dimensional results for average gas holdup within experimental error. A grid resolution study was done for the two-dimensional simulations and it was assumed that the three-dimensional simulations would use the same resolution. This assumption along with the use of a constant effective bubble diameter could lead to larger errors in three-dimensions.

The flow field predicted using two-dimensional simulations of the airlift reactor showed a regular oscillation of the gas flow due to flow recirculating from the downcomer and connectors, whereas the bubble column oscillations were random and resulted in flow moving through the center of the column. The profiles of gas holdup, gas velocity, and liquid velocity versus column width showed that the airlift reactor flow is asymmetric and the profile shape varied along the height of the column. The bubble column flow became independent of height after 20 cm above the inlet because there was less mixing than the airlift reactor. It was shown that the airlift reactor increased the mixing of the gas-liquid flow due to the addition of the downcomer. The airlift reactor showed less gas holdup in the riser than the bubble column but its velocity and gas holdup never became independent of column diameter like in the bubble column. The gas and liquid flow field of the two-dimensional airlift reactor was discussed and showed increased mixing with increasing inlet velocity.

The airlift reactor was simulated in both two- and three-dimensional geometries. The

three-dimensional simulations showed less oscillation throughout the riser due to the added azimuthal component. The flow in the large riser ($D_r = 10.2$ cm) was not as affected by the flow to and from the small connectors ($D = 2.4$ cm) in three-dimensions as it was in the two-dimensional model. Due to the azimuthal expansion, the three-dimensional flow also occupied more available area than the two-dimensional simulations, resulting in larger gas holdup predictions. When compared to experimental results [3], the three-dimensional simulations showed more realistic predictions of gas holdup than the two-dimensional simulations. The average riser gas holdup for the three-dimensional simulations were within experimental error, and the two-dimensional simulations underpredicted the average gas holdup. The velocity profiles for the two-dimensional and three-dimensional simulations showed that the solutions of both geometries were of similar magnitude.

## 5.2 Recommendations for Future Work

The predicted results were limited by the models used. One of the main limitations was the ability to model one bubble size. Implementation of the population balance model (PBM) of FLUENT was attempted, however due to stability issues, converged solutions were not attainable. Possible reasons for the instability are time step and cell size; more studies would have to be performed in order to fully assess the issues. The PBM is useful in that it does not necessitate estimating the proper characteristic bubble size but rather permits a specified bubble size distribution. Furthermore, the PBM considers the growth, breakup, and coalescence of bubbles to properly populate the bed. From the results provided in Chapters 3 and 4, the PBM could benefit the three-dimensional bubble column model and the two-dimensional airlift reactor model results the most. Future work would expand upon this to further understand the use of such a model.

The flow regime map of Chapter 3 was adapted from studying bubble columns [2].

It is unknown whether an airlift reactor will have the same transition parameters. A similar study to that of section 3.2 on varying the riser diameter of an airlift reactor can be performed to determine how well the two types of reactors correspond to each other spatially.

The purpose of these studies was to correctly model the hydrodynamics of the reactors. Models of fluids with similar physical characteristics (e.g., density, viscosity) but different chemical composition can be studied to predict reactions. Jones [3] was also able to perform experiments of KCl and Nitrosomonas solutions and measure mass transfer of oxygen and carbon monoxide. Other steps to further this research will include being able to model these reactions computationally using the same software as the hydrodynamic studies (FLUENT).

# Bibliography


[1] ANSYS, Inc, 2009, *ANSYS FLUENT 12.0 Theory Guide*.

[2] Shah, Y. and Deckwer, W., 1983, "Hydrodynamics of bubble columns," *Handbook of Fluids in Motion*, Ann Arbor Science, pp. 583–620.

[3] Jones, S. T., 2007, *Gas-liquid mass transfer in an external airlift loop reactor for syngas fermentation*, Ph.D. thesis, Iowa State University.

[4] Weiland, P. and Onken, U., 1981, "Fluid Dynamics and Mass Transfer in an Airlift Fermenter with External Loop," German Chemical Engineering, **4**(1), pp. 42–50.

[5] Prince, M. and Blanch, H., 1990, "Bubble Coalescence and Break-up in Air-Sparged Bubble-Columns," AICHE Journal, **36**(10), pp. 1485–1499.

[6] Jakobsen, H. A., Lindborg, H., and Dorao, C. A., 2005, "Modeling of bubble column reactors: Progress and limitations," Industrial and Engineering Chemistry Research, **44**(14), pp. 5107–5151.

[7] Sato, Y., Sadatomi, M., and Sekoguchi, K., 1981, "Momentum and haet transfer in two-phase bubble flow– I. Theory," International Journal of Multiphase Flow, **7**(2), pp. 167–177.

[8] Sokolichin, A. and Eigenberger, G., 1994, "Gas–liquid flow in bubble columns and loop reactors: Part I. Detailed modelling and numerical simulation," Chemical Engineering Science, **49**(24, Part 2), pp. 5735 – 5746.

[9] Sokolichin, A. and Eigenberger, G., 1999, "Applicibility of the standard $k-\epsilon$ turbulence model to the dynamic simulation of bubble columns: Part I. Detailed numerical simulations," Chemical Engineering Science, **54**, pp. 2273–2284.

[10] Lopez de Bertodano, M., Lahey Jr, R. T., and Jones, O. C., 1994, "Phase distribution in bubble two-phase flow in vertical ducts," International Journal of Multiphase Flow, **20**(5), pp. 805 – 818.

[11] Politano, M., Carrica, P., and Converti, J., 2003, "A model for turbulent polydisperse two-phase flow in vertical channels," International Journal of Multiphase Flow, **29**(7), pp. 1153 – 1182.

[12] Schwarz, M. and Turner, W., 1988, "Applicability of the standard $k-\epsilon$ turbulence model to gas-stirred baths," Applied Mathematical Modelling, **12**(3), pp. 273–279.

[13] Monahan, S., Vitankar, V., and Fox, R., 2005, "CFD predictions for flow-regime transitions in bubble columns," AICHE Journal, **51**(7), pp. 1897–1923.

[14] Law, D., 2010, *Computational Modeling And Simulations Of Hydrodyanmics For Air-Water External Loop Airlift Reactors*, Ph.D. thesis, Virginia Polytechnic Institute and State University.

[15] Law, D., Battaglia, F., and Heindel, T., 2006, "Numerical Simulations of Gas-Liquid Flow Dynamics in Bubble Columns," *Proceedings of 2006 ASME International Mechanical Engineering Congress and Exposition*, pp. 593–600.

[16] Rampure, M., Buwa, V., and Ranade, V., 2003, "Modelling of gas-liquid/gas-liquid-solid flows in bubble columns: Experiments and CFD simulations," Canadian Journal Of Chemical Engineering, **81**(3-4), pp. 692–706.

[17] Law, D., Battaglia, F., and Heindel, T., 2008, "Model validation for low and high

superficial gas velocity bubble column flows," Chemical Engineering Science, **63**(18), pp. 4605–4616.

[18] Glover, G. and Generalis, S., 2004, "The modelling of buoyancy driven flow in bubble columns," Chemical Engineering And Processing, **43**(2), pp. 101–115.

[19] Sari, S., Ergun, S., Barik, M., Kocar, C., and Sokmen, C. N., 2009, "Modeling of isothermal bubbly flow with interfacial area transport equation and bubble number density approach," Annals of Nuclear Energy, **36**(2), pp. 222–232.

[20] Simcik, M., Ruzicka, M., and Drahos, J., 2008, "Computing the added mass of dispersed particles," Chemical Engineering Science, **63**(18), pp. 4580–4595.

[21] Ranade, V. and Tayalia, Y., 2001, "Modelling of fluid dynamics and mixing in shallow bubble column reactors: influence of sparger design," Chemical Engineering Science, **56**(4), pp. 1667–1675.

[22] Gavrilescu, M. and Tudose, R., 1996, "Effects of downcomer-to-riser cross sectional area ratio on operation behaviour of external-loop airlift bioreactors," Bioprocess Engineering, **15**(2), pp. 77–85.

[23] Vial, C., Poncin, S., Wild, G., and Midoux, N., 2002, "Experimental and theoretical analysis of the hydrodynamics in the riser of an external loop airlift reactor," Chemical Engineering Science, **57**(22-23), pp. 4745–4762.

[24] Chen, P., Sanyal, J., and Dudukovic, M., 2004, "CFD modeling of bubble columns flows: implementation of population balance," Chemical Engineering Science, **59**(22-23), pp. 5201–5207.

[25] Sanyal, J., Marchisio, D., Fox, R., and Dhanasekharan, K., 2005, "On the Comparison between Population Balance Models for CFD Simulation of Bubble Columns," Industrial & Engineering Chemistry Research, **44**(14), pp. 5063–5072.

[26] Schiller, L. and Naumann, A., 1933, "Uber die grundlegenden berechnungen bei der schwerkraftaufbereitung," Zeitung des vereins deutscher ingenieure, pp. 77–318.

[27] Drew, D. A. and Passman, S. L., 1999, *Theory of Multicomponent Fluids*, Springer.

[28] Ferziger, J. and Peric, M., 2002, *Computational Methods for Fluid Dynamics*, Springer, 3rd ed.

[29] Tannehill, J. C., Anderson, D. A., and Pletcher, R. H., 1997, *Computational Fluid Mechanics and Heat Transfer*, Taylor and Francis, 2nd ed.

[30] Gerald, C. F. and Wheatley, P. O., 1999, *Applied Numerical Analysis*, Addison-Wesley, 6th ed.

[31] Dr. Christopher Roy, 2008, *Introduction to Computational Fluid Dynamics*.

[32] Shah, Y., Kelkar, B., Godbole, S., and Deckwer, W., 1982, "Design Parameters Estimations For Bubble Column Reactors," AICHE Journal, **28**(3), pp. 353–379.

[33] Dudukovic, M. P., Larachi, F., and Mills, P. L., 2002, "Multiphase catalytic reactors: a perspective on current knowledge and future trends," Catalysis Reviews: Science & Engineering, **44**(1), pp. 123–246.

[34] Govier, G. W., 1972, *The flow of complex mixtures in pipes*, Van Nostrand Reinhold Co.

[35] ANSYS, Inc, 2009, *ANSYS FLUENT 12.0 User's Guide*.

[36] Chen, P., Dudukovic, M., and Sanyal, J., 2005, "Three-dimensional simulation of bubble column flows with bubble coalescence and breakup," AICHE Journal, **51**(3), pp. 696–712.

[37] Law, D., Battaglia, F., and Heindel, T., 2008, "Simulating Gas-Liquid Flows in an External Loop Airlift Reactor," *ASME International Mechanical Engineering Congress and Exposition, IMECE 2008*, pp. 395–403.

[38] Blazej, M., Glover, G. C., Generalis, S., and Markos, J., 2004, "Gas-liquid simulation of an airlift bubble column reactor," Chemical Engineering and Processing, **43**(2), pp. 137–144.